Geoscience Frontiers 12 (2021) 101171

Contents lists available at ScienceDirect

Geoscience Frontiers

journal homepage: www.elsevier.com/locate/gsf

Research Paper

Modeling the multi-level plumbing system of the Changbaishan caldera from geochemical, mineralogical, Sr-Nd isotopic and integrated geophysical data

Jian Yi [a,b], Pujun Wang [a,b], Xuanlong Shan [a,b,*], Guido Ventura [c,d], Chengzhi Wu [e], Jiannan Guo [a,b], Pencheng Liu [a,b], Jiahui Li [a,b]

[a] College of Earth Science, Jilin University, Jianshe Street 2199, Changchun 130061, China
[b] Key Laboratory for Evolution of Past Life and Environment in Northeast Asia (Jilin University), Ministry of Education, Changchun 130026, China
[c] Istituto Nazionale di Geofisica e Vulcanologia, Via di Vigna Murata, 605, Roma 00143, Italy
[d] Istituto per lo Studio degli impatti Antropici e Sostenibilità in ambiente marino (IAS), Capo Granitola (TP) 91021, Italy
[e] Changbai Mountain Tianchi Volcano Observatory, Chibei District, Antu 133613, China

ARTICLE INFO

Article history:
Received 16 August 2020
Received in revised form 21 January 2021
Accepted 7 February 2021
Available online 17 February 2021

Handling Editor: S. Ganguly

Keywords:
Changbaishan volcano
Caldera
Plumbing system
Triggering mechanism
Storage depth

ABSTRACT

Changbaishan, an intraplate volcano, is characterized by an approximately 6 km wide summit caldera and last erupted in 1903. Changbaishan experienced a period of unrest between 2002 and 2006. The activity developed in three main stages, including shield volcano (basalts), cone-construction (trachyandesites to trachytes with minor basalts), and caldera-forming stages (trachytes to comendites). This last stage is associated with one of the more energetic eruptions of the last millennium on Earth, the 946 CE, VEI 7 Millennium Eruption (ME), which emitted over 100 km^3 of pyroclastics. Compared to other active calderas, the plumbing system of Changbaishan and its evolution mechanisms remain poorly constrained. Here, we merge new whole-rock, glass, mineral, isotopic, and geobarometry data with geophysical data and present a model of the plumbing system. The results show that the volcano is characterized by at least three main magma reservoirs at different depths: a basaltic reservoir at the Moho/lower crust depth, an intermediate reservoir at 10–15 km depth, and a shallower reservoir at 0.5–3 km depth. The shallower reservoir was involved in the ME eruption, which was triggered by a fresh trachytic melt entering a shallower reservoir where a comenditic magma was stored. The trachytes and comendites originate from fractional crystallization processes and minor assimilation of upper crust material, while the less evolved melts assimilate lower crust material. Syn-eruptive magma mingling occurred during the ME eruption phase. The magma reservoirs of the caldera-forming stage partly reactivate those of the cone-construction stage. The depth of the magma storage zones is controlled by the layering of the crust. The plumbing system of Changbaishan is vertically extensive, with crystal mush reservoirs renewed by the replenishment of new trachytic to trachyandesitic magma from depth. Unlike other volcanoes, evidence of a basaltic recharge is lacking. The interpretation of the signals preceding possible future eruptions should consider the multi-level nature of the Changbaishan plumbing system. A new arrival of magma may destabilize a part of or the entire system, thus triggering eruptions of different sizes and styles. The reference model proposed here for Changbaishan represents a prerequisite to properly understand periods of unrest to potentially anticipate future volcanic eruptions and to identify the mechanisms controlling the evolution of the crust below volcanoes.

1. Introduction

Calderas are assumed to be characterized by complex plumbing systems consisting of multiple, partly superimposed, sill-like crystal-mush where repeated recharge episodes and mixture of magmas occur (De Silva et al., 2008; Myers et al., 2014; Hernando et al., 2016; Cashman et al., 2017; Kennedy et al., 2018). Kruger and Latypov (2020) proposed an alternative model in which the chemical zoning is related to solidification fronts at the chamber floor, a process responsible for fractionation due to convective removal of a compositional boundary layer. This model suggests that magma reservoirs are more consistent with a classical, single-chamber, crystal-poor and liquid-rich model. More complex growths of the plumbing systems of calderas have been also proposed (Geyer et al., 2006, 2019; Kennedy et al., 2018)—e.g., at Campi Flegrei (Italy), where an early large, single magma chamber responsible for caldera-forming eruptions evolved with time to a

* Corresponding author at: College of Earth Science, Jilin University, Jianshe Str. 2199, 130061 Changchun, China.
E-mail address: Shanxl@jlu.edu.cn (X. Shan).

https://doi.org/10.1016/j.gsf.2021.101171

vertically extensive system consisting of different sill-like reservoirs (Forni et al., 2018). Another example is Deception Island (South Shetland Islands), which is one of the most active volcanoes in Antarctica. New petrologic and geochemical work reveal the existence of a complex plumbing system composed of several shallow magma chambers (≤10 km depth) fed by magmas raised directly from the mantle, or from a magma accumulation zone located at the crust-mantle boundary (15–20 km depth) (Geyer et al., 2019). The above reported views of the inner structure of volcanoes and their evolution over time represent a topic of primary importance to understanding (a) the structure of the plumbing system, (b) how the volcano works, and (c) its future evolution. These latter two topics are of primary importance for constructing a reference model that correctly interprets monitoring data from active calderas and the related hazard evaluation. In addition, calderas are responsible for the more energetic eruptions that have occurred on Earth, which include the circa 1 ka old Millennium eruption at Changbaishan volcano (China/North Korea). These large-scale events may alter the climate at a global scale, but their eruptive dynamics, their triggering mechanisms and the plumbing system of volcanoes able to produce such devastating eruptions remain poorly understood (Mason et al., 2004; Costa et al., 2018; Papale and Marzocchi, 2019). In addition, our ability to forecast future, large-scale eruptions from monitoring data represents a challenge of modern volcanology because a reference model of many super-volcanoes is, at present, lacking or poorly constrained. The Changbaishan intraplate volcano, also named Paektu, Baekdu, and Tianchi, is located, as previously reported, at the China/North Korea boundary and reaches 2774 m above sea level. Changbaishan is characterized by a summit and sub-circular caldera depression with a radius of approximately 2.8 km and is filled by Heaven Lake; the last eruption occurred in 1903. Changbaishan is considered one of the most dangerous active volcanoes of Eastern Asia because it was responsible for the VEI 7 Millennium eruption (ME) in 946 ± 20 CE (Fig. 1) (Liu and Wang, 1982; Hetland et al., 2004; Wei et al., 2013; Xu et al., 2013). ME produced a large volume of tephra (77–172 km^3) including falls, pyroclastic flows, lahars, and gas emissions with a global climatic impact (Horn and Schmincke, 2000; Guo

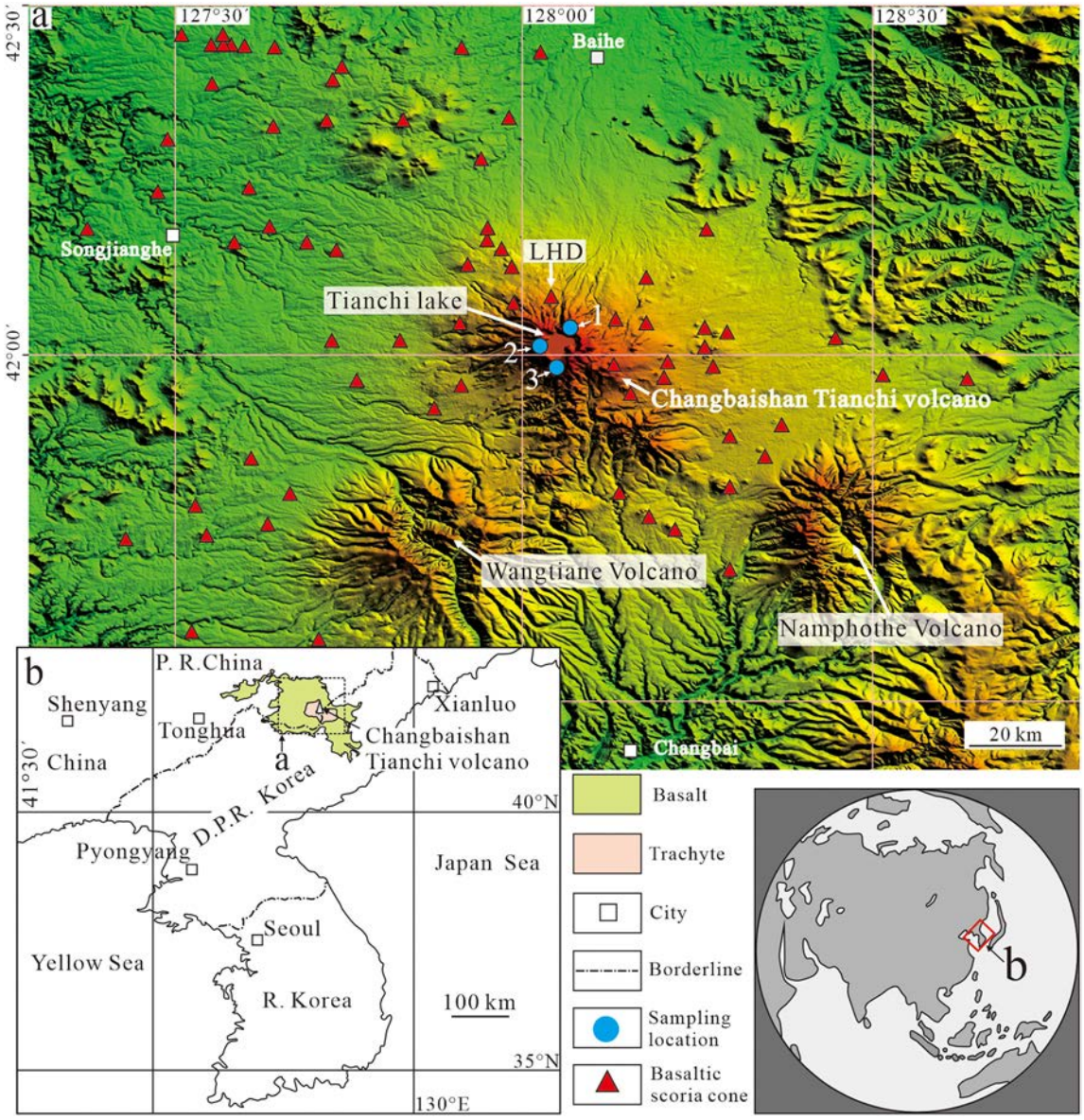

Fig. 1. (a) Map of Changbaishan Tianchi Volcano and the sampling locations. (b) Overview map showing the location of Changbaishan volcano. Sampling location: (1) The five main pumice accumulation units (U1 to U5) of the caldera-forming stage at the Tianwen Summit; (2) light gray pumice of U3 on the west slope of the volcanic cone; (3) light gray pumice of U3 on the south slope of the volcanic cone. LHD: Laohudong basaltic scoria cone.

et al., 2002, 2006; Xu et al., 2013; Sun et al., 2014a, 2014b; Yi et al., 2019). Monitoring data are recorded by the Changbaishan Volcano Observatory, and an unrest episode characterized by deformations, earthquakes, and changes in volcanic gas geochemistry occurred between 2002 and 2006 (Xu et al., 2012). The Changbaishan products include early basalts, trachyandesites, and later trachytes and rhyolites (comendites) (Liu, 1987; Jin and Zhang, 1994; Zhang et al., 2018). In the Holocene, the activity changed from a cone-construction stage with trachytic lava effusions to a caldera-forming stage characterized by Plinian eruptions (the 4 ka TWF eruption and the ME eruption; Wei et al., 2013; Sun et al., 2017, 2018). Reconstruction of the Changbaishan magma evolution processes and of the structure of the plumbing system during the caldera-forming stage allow us to better constrain the mechanisms responsible for the large eruptions at this volcano and evaluate the associated volcanic hazard.

Previous geochemical and mineralogical studies on the Changbaishan products indicate that almost all the erupted, evolved magmas derive from the fractionation of a basaltic parental magma originating in the upper mantle (Li et al., 2004; Andreeva et al., 2014; Liu et al., 2015; Pan et al., 2017a, 2017b; Zhang et al., 2018). The trachytic and comenditic pumices of the caldera-forming stage are considered to have evolved from the trachyandesitic and trachytic magmas of the cone-construction stage by fractional crystallization processes in the middle crust (Li et al., 2004; Andreeva et al., 2018; Zhang et al., 2018). However, the SiO_2 content of the products of the caldera-forming stage does not monotonically increase from the early to the late eruptions but fluctuates with time (Fig. 2a). This behavior does not conform to a classical fractional crystallization model in a single magma chamber and suggests the occurrence of multiple reservoirs in which magmas may evolve independently (Geyer et al., 2006, 2019; Pan et al., 2017a). Pan et al. (2017a, 2017b) demonstrated magma mingling between trachytes and comendites in the ME products and suggested that two types of magmas upraise from different reservoirs during this eruption. Combined with the previously described fluctuations in SiO_2 content during the Changbaishan caldera-forming stage (Fig. 2a), a complex plumbing system is assumed to be present beneath the caldera. However, the

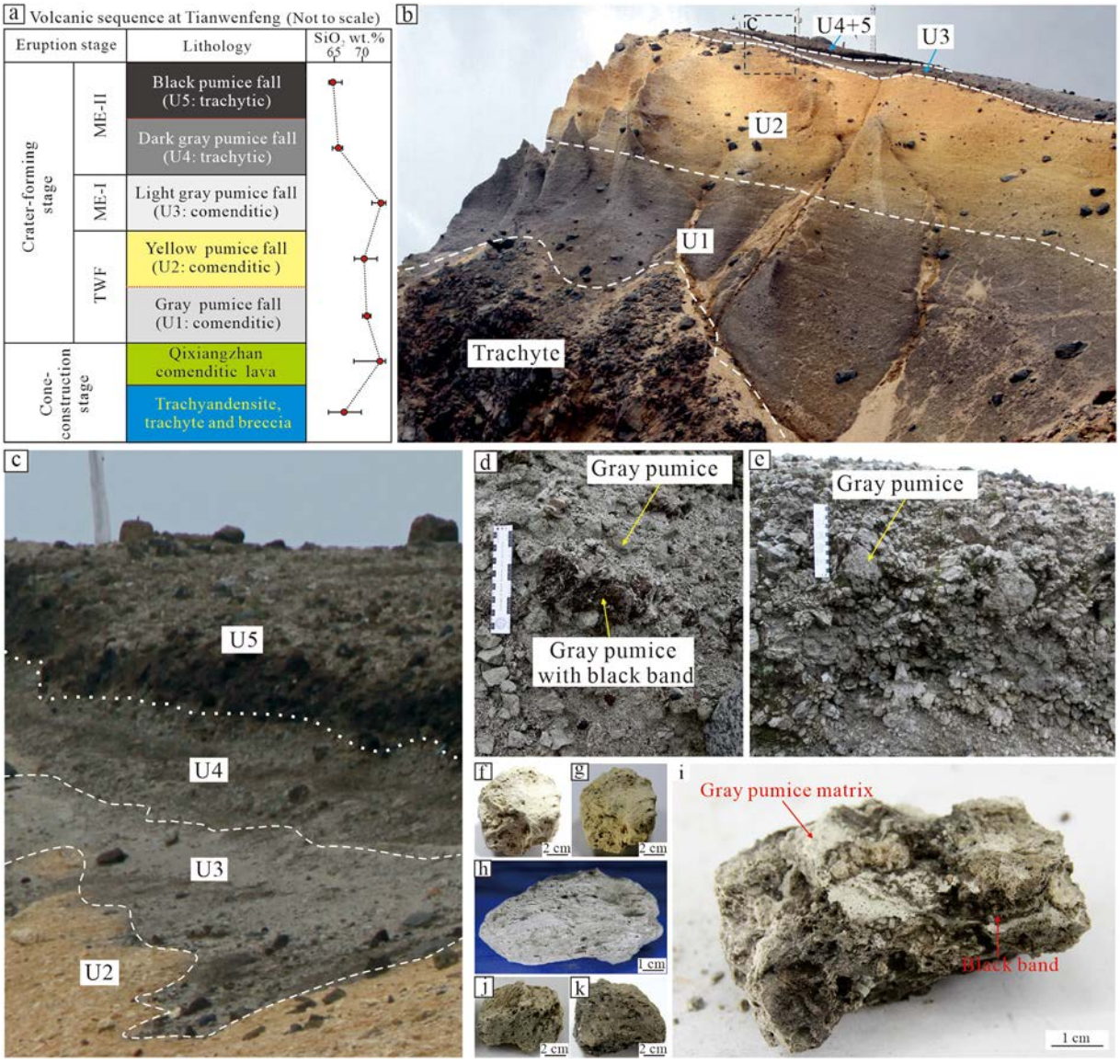

Fig. 2. (a) Volcanic succession at the Tianwen Summit. (b) Photograph showing the five main eruptive units (U1 to U5) of the caldera-forming stage at the Tianwen summit (Number 1 in Fig. 1). (c) Locally enlarged photograph showing pumice accumulations from U2 to U5. (d) Light gray pumice of ME-I (U3) at the south slope summit (Number 2 in Fig. I) showing some gray pumices with black bands. (e) Light gray pumice of ME-I (U3) at the west slope summit (Number 3 in Fig. I). (f) Gray pumice of U1. (g) Yellow pumice of U2. (h) Light gray pumice of U3. (i) Light gray pumice with black band in U3. (j) Dark gray pumice of U4. (k) Black pumice of U5.

structure of this plumbing system and the magma evolution processes remain poorly understood.

In this study, we systematically analyzed the geochemistry, mineral composition, and Sr-Nd isotopes of the five main units of the caldera-forming stage and integrated these data with the available geophysical information. Our aim was to model the structure and the magmatic evolution processes of the plumbing system beneath the Changbaishan volcano in the caldera-forming stage.

2. Geological background and sampling

The Changbaishan intraplate volcano is associated with a mantle upwelling developing above the 500–600 km deep flat slab related to the subduction of the Pacific plate below the northeastern Asian mainland (Dostal et al., 1988; Zhao and Liu, 2010; Lei et al., 2013; Kern et al., 2016). The Changbaishan eruptive history can be divided into three main stages: the shield-forming stage, the cone-construction stage, and the caldera-forming stage (Liu and Wang, 1982; Liu et al., 1992; Machida et al., 1990; Liu and Xiang, 1997; Zhang et al., 2018). The large Gaima basalt plateau, which represents the basement over which Changbaishan grew, developed during the shield-forming stage between 22.6 Ma and 1.1 Ma. The Changbaishan cone activity, which mostly consists of trachyandesites and trachytes, occurred at 1.37 Ma (Sun et al., 2017; Zhang et al., 2018), and the Qixiangzhan comenditic lava flow (QXZ comenditic lava), which erupted at 17 ka, was the last eruption event of the cone-construction stage (Singer et al., 2014). The caldera-forming stage (0.01 Ma to 946 CE) produced trachytic-comenditic pumices during Plinian eruptions (Sun et al., 2017; Zhang et al., 2018). At the Tianwenfeng summit near caldera lake, a typical outcrop includes the five main pumice units (U1 to U5) of the caldera-forming stage (Figs. 1aand Fig. 2a–c). The pumices of U1 (gray, e.g., Fig. 2f) and U2 (yellow, e.g., Fig. 2g) have different colors but similar comenditic composition. There is no clear stratigraphic gap between the two units; the color of pumices gradually changes, moving upwards from gray to light gray and light yellow and then to yellow (Fig. 2b). Lacking stratigraphic gaps—e.g., paleosoils—or significant unconformities, U1 and U2 most likely formed during one nearly continuous eruption event (Sun et al., 2017; Zhang et al., 2018). Sun et al. (2017) named this event the TWF eruption, which, based on ^{40}Ar-^{39}Ar dating, occurred circa 4 ka (Yang et al., 2014). According to Horn and Schmincke (2000) and Pan et al. (2017a, 2017b), the VEI 7, ME event can be divided into two main eruption phases: an earlier, large-scale eruption phase I (ME-I) and the later eruption phase II (ME-II) (Fig. 2a). In the section at the Tianwenfeng summit, the light gray comenditic pumice of U3 (e.g., Fig. 2h) is considered to have formed during ME-I; the dark gray pumice of U4 (e.g., Fig. 2j) and the black pumice of U5 (e.g., Fig. 2k) have a trachytic composition and lack clear stratigraphic discontinuities. U4 and U5 are here considered to have formed during ME-II (Sun et al., 2017; Zhang et al., 2018) (Fig. 2a and c). In U3, some light gray pumice of ME-I has black bands in the matrix (Fig. 2d, i). Pan et al. (2017 a, 2017b, 2020) demonstrated that the black bands have a composition similar to that of the dark gray and black trachytic pumices of ME-II, and the magmas of ME-I and ME-II mingle during ME.

3. Analytical methods

Samples of pumice from U1 to U5 (Fig. 2b and c) were collected at the Tianwen summit of Changbaishan, and the light gray pumice of ME-I (U3) was collected from the south and west slope summits (Fig. 2d and e). These samples were selected for geochemical, mineralogical, and Sr-Nd isotopic analyses (Table 1).

The samples for the whole-rock geochemical analyses were crushed in an agate mill and passed through ~200 mesh sieves. X-ray fluorescence (XRF; Rigaku RIX 2100 spectrometer) was used to determine the major elemental compositions, and inductively coupled plasma mass spectrometry (ICP-MS) (Agilent 7500a with a shield torch) was used to analyze the trace elements at the Key Laboratory of Mineral Resources Evaluation in Northeast Asia (Ministry of National Resources of the People's Republic of China, Jilin University, Changchun, China). The analytical precision for major elements was better than 3%, and that for trace elements was better than 5%.

The samples selected for mineral and glass compositional microanalysis were prepared on thin sections and coated with carbon films. Chemical microanalysis of minerals and glass was performed at the State Key Laboratory of Ore Deposit Geochemistry (Chinese Academy of Sciences at Guiyang) with a JXA8230 microprobe and at the Key Laboratory of Mineral Resources Evaluation in Northeast Asia (Ministry of National Resources of the People's Republic of China in Jilin University, Changchun, China) with a JXA8230 microprobe. The operating conditions of the microprobe were 25 kV of accelerating voltage, a sample current of 10 nA, and a 1–10 μm electron beam according to the size of the mineral and glass shards. The analytical uncertainties were less than 2%.

Powered whole-rock samples were used for the Sr-Nd isotopic determinations. The Sm-Nd and Rb-Sr analyses were carried out at the Laboratory for Radiogenic Isotope Geochemistry, University of Science and Technology of China (USTC) following the methods of Chen et al. (2000). The isotopic ratios were determined on a Finnigan MAT 262 instrument (USTC) and an upgraded MAT261 mass spectrometer (LMU). Sr and Nd isotopic ratios were corrected for mass fractionation relative to $^{86}Sr/^{88}Sr = 0.1194$ and $^{146}Nd/^{144}Nd = 0.7219$, respectively. Analyses on the standard solutions of NBS 987 and La Jolla standards yielded mean values of 0.710249 ± 0.000012 (2σ, $n = 38$) for $^{87}Sr/^{86}Sr$ and 0.511869 ± 0.000006 (2σ, $n = 25$) for $^{143}Nd/^{144}Nd$.

4. Results

We systematically analyzed the petrography, whole-rock chemistry, Sr-Nd isotopes, and minerals of pumices U1 to U5. Geochemical and mineral chemistry data of the Changbaishan basic to intermediate volcanic rocks of the shield-forming stage and cone-construction stage are from Li et al. (2004), Liu et al. (2015), Chen et al. (2017) and Zhang et al. (2018).

Table 1
Samples for geochemical, Sr-Nd isotopic and mineral analysis.

Unit	Sample	Lithology	Location
U1	TwF-2a, TwF-2b, TwF-1a, TwF-1b, TwF-1c, TwF-0	Gray comenditic pumices	Tianwen summit
U2	TwF-3a, TwF-3b, TwF-3c, TCB-7, TCB-3a, TCB-3b, TCB-3c, TCB-5Y	Yellow comenditic pumices	Tianwen summit
U3	TCB-8	Little gray comenditic pumices	Tianwen summit
	TCN-7 W, TCN-4 W, TCN-1 W	Little gray comenditic pumices	South slope summit
	TCN-6 W		
	TCN-1, TCN-18a, TCN-18b	Little gray comenditic pumices	West slope summit
U4	TCB-1a, TCB-1b, TCB-2a, TCB-2b, TCB-2c	Dark gray trachytic pumices	Tianwen summit
U5	TCB-6-1, TCB-6-2, TCB-6-3, TCB-6-4, TCB-6-5	Black trachytic pumices	Tianwen summit

4.1. Petrography and whole-rock geochemistry

Major and trace element geochemistry data for the pumice from U1 to U5 are reported in Supplementary Tables S1 and S2. Fig. 3 shows the compositions of Changbaishan alkaline rocks.

4.1.1. Gray pumicesU1

The gray pumices in U1 show a comenditic composition (Fig. 3). The pumices are subaphyiric with approximately 3 vol% of phenocryst fragments (Fig. 4a). The phenocryst fragments consist of alkali feldspars (approximately 2 vol%), clinopyroxene (<1 vol%) and olivine (<1 vol%).

4.1.2. Yellow pumice U2

The yellow pumices in U2 mainly present a comenditic composition similar to that of the gray pumice in U1 (Fig. 3). The pumices in U2 contain a few phenocrysts (<5 vol%) consisting of alkali feldspars (3–4 vol %), clinopyroxene (< 1 vol%) and olivine (< 1 vol%) (Fig. 4b). Vitric ash with phenocryst fragments in the yellow pumice at the base of U2 has been also recognized.

4.1.3. Light gray pumice U3

The light gray pumice in U3 has a comenditic composition. It is poor in phenocrysts (< 1 vol%) with feldspar and clinopyroxene (Fig. 4c). In this unit, some banded black and light gray pumices occur (Figs. 2i and 4d). In the black bands, the phenocrysts (embayed alkali feldspar, clinopyroxene and olivine) are more abundant than in the glassy matrix of the light gray pumice (Fig. 4d).

4.1.4. Dark gray and black pumices U4 and U5

The dark gray and black pumices in U4 and U5 have a similar trachytic composition (Fig. 3). The black pumice has the lowest SiO_2 content (SiO_2 = 63.8–64.2 wt.%) among the juvenile clasts of the studied five units; the SiO_2 content of the dark gray pumice (SiO_2 = 64.5–66.2 wt.%) in U4 is slightly higher than that of the dark pumice in U5. Generally, the juvenile clasts in U4 and U5 have similar petrographic characteristics. They are poor in phenocrysts (< 5 vol%) with alkali feldspars (3–4 vol%), clinopyroxene (<1 vol%) and olivine (<1 vol%). The glass matrix of the pumices in U4 and U5 is brown (Fig. 4e and f).

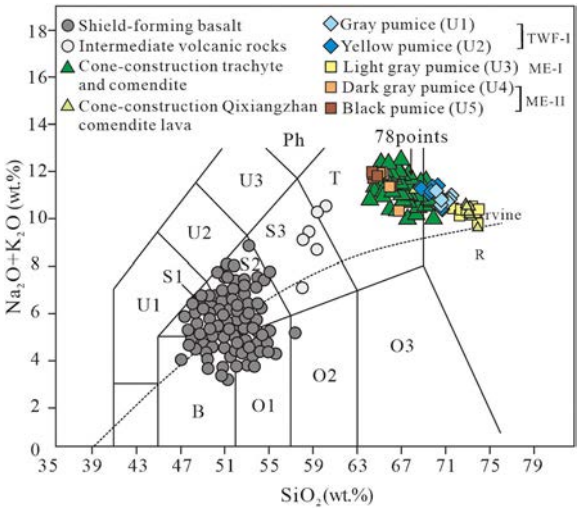

Fig. 3. $Na_2O + K_2O$ versus SiO_2 diagram for the Changbaishan Tianchi volcano. All plotted data were recalculated to 100 wt.% on a volatile-free basis. Classification boundaries are from Le Bas et al. (1986) and Le Maitre et al. (1989). Boundary line for alkaline and subalkaline magma series is from Irvine and Baragar (1971). The data for the shield-forming basalt, intermediate volcanic rocks and cone-construction trachyte of the Changbaishan volcano are from Liu et al. (2015) and Zhang et al. (2018). Rock types: B, basalt; S1, trachybasalt; S2, basaltic trachyandesite; S3, trachyandesite; T, trachyte; U1, tephrite; U2, phonotephrite; U3, tephriphonolite; Ph, phonolite; O1, basaltic andesite; O2, andesite; O3, dacite; R, rhyolite.

In summary, the pumices of U1 to U5 display repeated fluctuations in SiO_2 content, and the pumices of U4 and U5, which represent the last eruption of the Changbaishan caldera-forming stage, show the lowest SiO_2 contents (Fig. 3). On the Harker diagrams for the selected major elements, the pumices of the caldera-forming stage describe evolution trends with the trachyte and trachyandesite of the cone-construction stage and the basalt of the shield-forming stage that are compatible with processes dominated by olivine, Fe-Ti oxides, clinopyroxene and alkali feldspar removal processes as a function of the different degrees of evolution of the involved magmas (Fig. 5). Harker variation diagrams for the selected trace elements show that, apart from some compatible elements (such as Eu and Co) that show a negative correlation, the other incompatible elements, such as Pb, Th, U, Ta, Nb and Rb, present a positive correlation with SiO_2 (Fig. 6).

The chondrite-normalized (Fig. 7a) and primitive mantle-normalized diagrams (Fig. 7b) show similar patterns for the volcanic rocks of the cone-construction stage: (a) strongly fractionated rare earth element (REE) patterns characterized by relative enrichments in light REEs (LREEs) and relative depletions in heavy REEs (HREEs); (b) a significant negative Eu anomaly; (c) large ion lithophile element (LILE; K and Rb), LREE, and high field strength element (HFSE; Nb and Ta) enrichments, slight HREE depletions, and strong negative Sr, Ba, P, and Ti anomalies. Although the patterns are generally similar, the total REEs and trace elements present relatively wide ranges and negative Eu, Sr, Ba, P, and Ti anomalies (Fig. 7a and b). As the degree of magma evolution increases, the total REEs and trace elements also increase with negative Sr, Ba, P, and Ti anomalies (Fig. 7a and b). The QXZ comenditic lava, which represents the more evolved product of the cone-construction stage, is characterized by the highest total REEs (Fig. 7a) and negative Eu, Sr, Ba, P, and Ti anomalies (Fig. 7b). For the caldera-forming stage, the pumices of U1 to U3 have patterns consistent with those of the QXZ comenditic lava in the chondrite-normalized diagram and the primitive mantle-normalized diagram (Fig. 7c–f). The pumices in U4 and U5 have lower REEs and smaller negative Eu, Sr, Ba, P, and Ti anomalies than the pumices in U1 to U3 and show patterns similar to those of the volcanic rocks with the lowest degree of evolution in the cone-construction stage (Fig. 7g and h).

4.2. Compositions of pumice glass and vitric ash

The composition of the glass matrixes of pumices from U1 to U5 is reported in Supplementary Table S3 and shown in Fig. 8. The composition of the glass matrix of the pumices and of the vitric ash depicts three distinct groups (Fig. 8). One group consists of the glass of the black and dark gray pumices of U5 and U4 and the black bands in the light gray pumice of U3. The second group consists of the glass matrix of the gray and yellow pumices of U1 and U2 and their corresponding vitric ash. The third group includes the glass of the light gray pumice of U3. The composition of the glass in banded pumices of U3 suggests mingling processes between the U4 and U5 magmas and the U1-U3 magmas.

4.3. Sr-Nd isotopes

In this study, the Sr and Nd isotopic determinations include the pumices from U1 to U5. The data are listed in Table 2. Combined with other available Sr-Nd isotopic data from the shield-forming basalts, cone-construction trachytes, and QXZ lava (Guo et al., 2016; Zhang et al., 2018), we report our new data in terms of $^{143}Nd/^{144}Nd$ vs $^{87}Sr/^{86}Sr$, $^{87}Sr/^{86}Sr$ vs SiO_2, $^{87}Sr/^{86}Sr$ vs Th and $^{87}Sr/^{86}Sr$ vs Age in Fig. 9. Fig. 9a demonstrates that the volcanic rocks of the cone-construction stage and caldera-forming stage have similar narrow ranges of $^{143}Nd/^{144}Nd$ and relatively wide ranges of $^{87}Sr/^{86}Sr$. These results indicate that the volcanic rocks of these two stages experienced

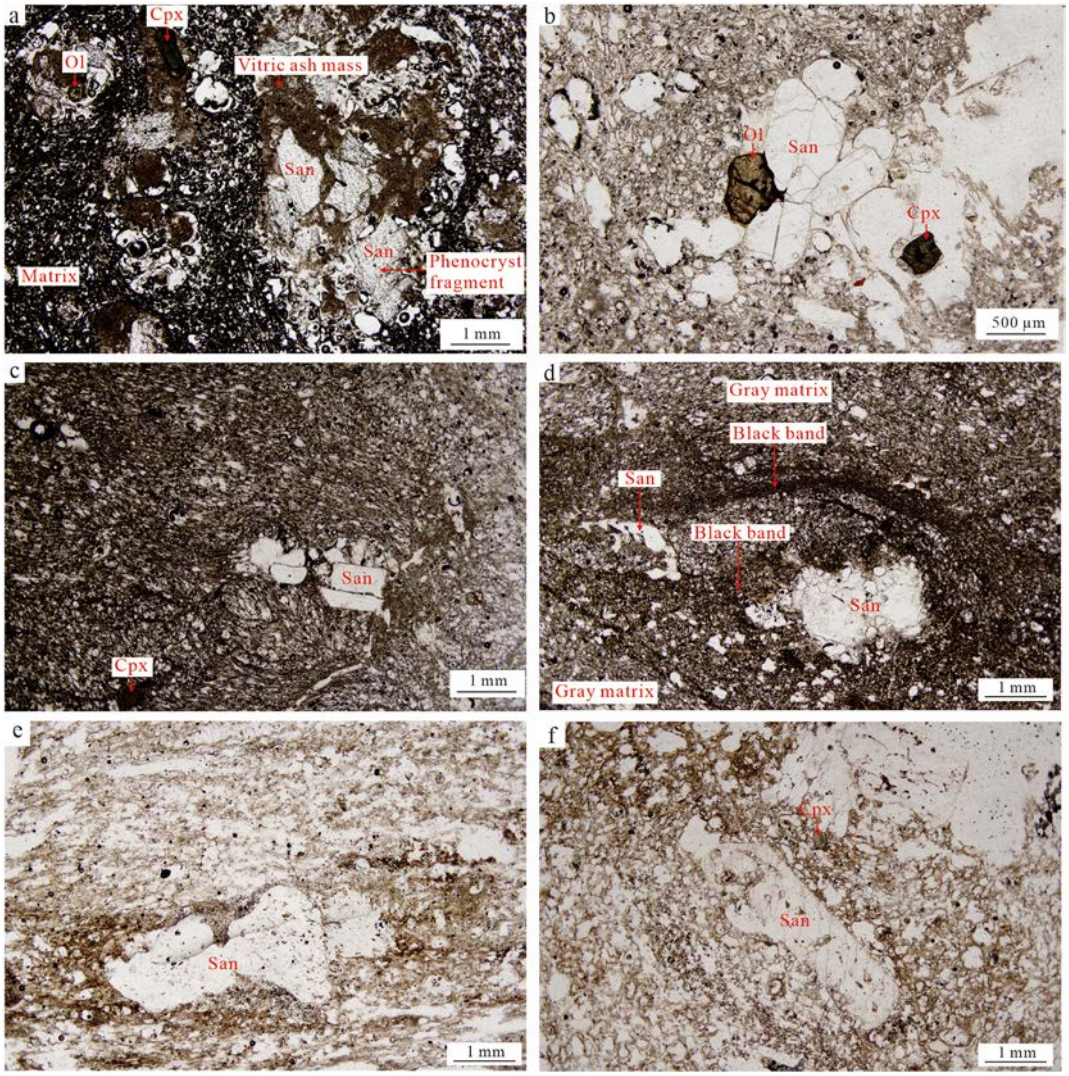

Fig. 4. Photomicrographs of the pumices from U1 to U5. (a) The gray pumice of U1 with some vitric ash masses and phenocryst fragments in the glass matrix. (b) The yellow pumice of U2. (c) The light gray pumice of U3. (d) The light gray pumice of U3 with black bands. (e) The dark gray pumice of U4. (f) The dark gray pumice of U5. San: sanidine; Cpx: clinopyroxene; Ol: olivine.

some interactions with upper crust material, as was also suggested by Guo et al. (2016). In the $^{87}Sr/^{86}Sr$ vs SiO_2 and $^{87}Sr/^{86}Sr$ vs Th diagrams (Fig. 9b and c), two main trends may be recognized: a high$^{87}Sr/^{86}Sr$ evolution trend defined by some cone-construction trachytes and the pumices of the U1 and U2 units, and a lower $^{87}Sr/^{86}Sr$ trend defined by the QXZ comenditic lava of the cone-construction stage and by the light gray pumice of U3. In addition, at the end of the low-$^{87}Sr/^{86}Sr$ assimilation trend, we can recognize another high-$^{87}Sr/^{86}Sr$ evolution trend linking the QXZ comenditic lava to pumice U3 (trend-II in Fig. 9b, c). Notably, the dark gray and black pumices of U4 to U5 are located at the intersection point of two above-described main trends (Fig. 9). In Fig. 9d, the high $^{87}Sr/^{86}Sr$ evolution trend appears earlier than the lower $^{87}Sr/^{86}Sr$ trend. In addition, trend-II separated into two lines, trend-II_a and trend-II_b, corresponding to the QXZ eruption and the ME-I eruption, respectively.

4.4. Mineral chemistry

We systematically analyze the composition from rim to core of phenocrysts including feldspars, pyroxene, and olivine in pumices U1 to U5. All mineral chemistry data are reported in Supplementary Tables S4–S6.

4.4.1. Feldspars

Based on the analysis of the feldspar compositions in pumices U1 to U5 (Supplementary Table S4), we identify four main groups of feldspar: Af1, Af2, Af3 and Pl1 (Table 3, Figs. 10 and 11). Af1 to Af3 are all alkali feldspars with a relatively homogeneous composition. Af1 is characterized by $An_{<0.5}$ with $Or_{34–40}$ and $Ab_{60–66}$ (Figs. 10 and 11). Af2 shows $An_{2–8}$ with $Or_{38–48}$ and $Ab_{48–57}$ (Figs. 10 and 11). Almost all Af3 crystals are anorthoclase with compositions of $An_{16–21}$, $Or_{21–26}$, and $Ab_{57–59}$ (Figs. 10 and 11). Pl1 is plagioclase with a large compositional heterogeneity from rims (andesine) to cores (labradorite) (Figs. 10 and 11). Table 3 reports the assemblage of feldspars in pumices U1 to U5. These results indicate that trachytic and comenditic pumices U1 to U3 have similar feldspar assemblages with Af1, except the yellow pumice U2, which has a small amount of Af2. The U4 and U5 trachytic pumices and the black bands in the light gray pumice U3 have the Af2, Af3 and Pl1 assemblages. The Af1 crystals are subhedral with clean surfaces in light gray pumice U3 and show a sieve texture in gray and yellow pumices U1 and U2. All Af2 and Af3 crystals are subhedral to anhedral with sieve dissolution textures and embayments. Pl1 in the black and dark gray pumices of U4 and U5 are characterized by a weak sieve dissolution texture (Table 3, Fig. 11).

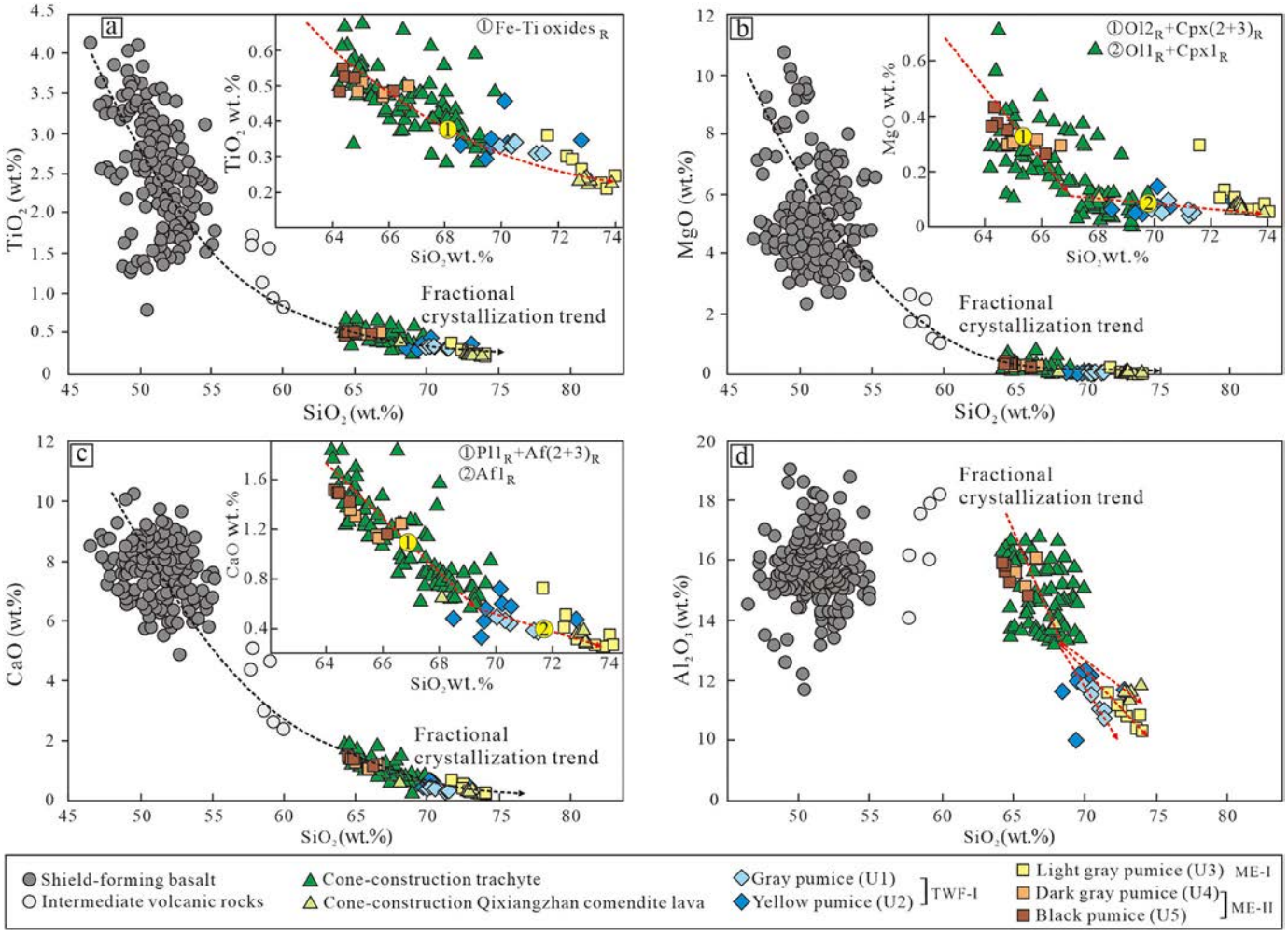

Fig. 5. Selected major element of whole-rock compositions. (a) TiO_2 (wt.%) versus SiO_2 (wt.%). (b) MgO (wt.%) versus SiO_2 (wt.%). (c) CaO (wt.%) versus SiO_2 (wt.%). (d) Al_2O_3 (wt.%) versus SiO_2 (wt.%). The geochemical data and mineral assemblage of the shield-forming basalts and intermediate volcanic rocks and the cone-construction trachyte and QXZ comenditic lava are from Liu et al. (2015) and Zhang et al. (2018). Af: alkali feldspar; Ol: olivine; Cpx: clinopyroxene; Subscript R: removal.

4.4.2. Pyroxenes

Three groups of clinopyroxene (Cpx1, Cpx2 and Cpx3) occur in pumices U1 to U5 (Table 3, Supplementary Table S5, Fig. 12). These three groups differ in Fs content with decreasing Fs from Cpx1 to Cpx3 (Fig. 12). Pumices U1 to U3 have Cpx1 pyroxenes. Cpx2 and Cpx3 are mainly found in black and dark gray pumices U4 and U5 and in the black bands of pumice U3. Almost all Cpx1 crystals are subhedral with clean surfaces, while the Cpx2 and Cpx3 are subhedral with sieve dissolution surfaces (Table 3, Fig. 12).

4.4.3. Olivine

There are two types of olivine phenocrysts (Ol1 and Ol2) in pumices U1 to U5 (Table 3, Fig. 13) (Supplementary Table S6). Ol1 is fayalite with very low Fo (Fo$_{<1.5}$), and Ol2 shows a higher Fo content (Fo$_{13-16}$). Ol1 is present in te gray and yellow pumices U1 and U2. Dissolution textures are common in Ol1 with crystals with rounded shape and embayment. Dark gray and black pumices U4 and U5 have Ol2 with sub-rounded shapes and embayment (Table 3, Fig. 13).

5. Discussion

In the following, we discuss our data in light of the available geochemical and geophysical information.

5.1. Depth of reservoirs in the caldera-forming stage

The storage depth of magmas is generally deduced based on the results of geobarometry determinations (Kennedy et al., 2018). Iacovino et al. (2016) calculated the magma storage depth of the ME-I (light gray pumice U3) from geobarometric determinations on melt inclusions; they found pressures between 0.15 and 0.90 kbar, which suggested depths between 0.5 and 3.5 km assuming an average crustal density of 2400 kg/m^3 (Iacovino et al., 2016). These depths are consistent with the low seismic velocity zone and the low resistivity anomalies found below Changbaishan (Stone, 2011; Qiu et al., 2014; Zhu et al., 2019). In addition, the hypocenters of the earthquakes recorded during the 2002–2005 unrest period are within the range of depths (Wu et al., 2007; Liu et al., 2011, 2017; Xu et al., 2012; Iacovino et al., 2016; Fig. 14). Here, we determine the depth of the magma storage zone(s) of the black and dark gray pumices U4 and U5 (Table 4) using an improved clinopyroxene-liquid equilibrium geobarometer that is specific to alkaline-differentiated magmas by Masotta et al. (2013) (Table 4) (this method was an improvement of and based on that of Putirka et al. (1996, 2003) and Putirka (2008). The obtained results indicate that magmas U4 and U5 had similar pressures: black pumice U5 gives a range of 0.7 to 0.8 kbar, and dark gray pumice U4 yields a range of 0.6–0.7 kbar (Table 4). The corresponding magma storage depths are 2.9 to 3.3 km for U5 and 2.5 to 2.9 km for U4 (Fig. 14).

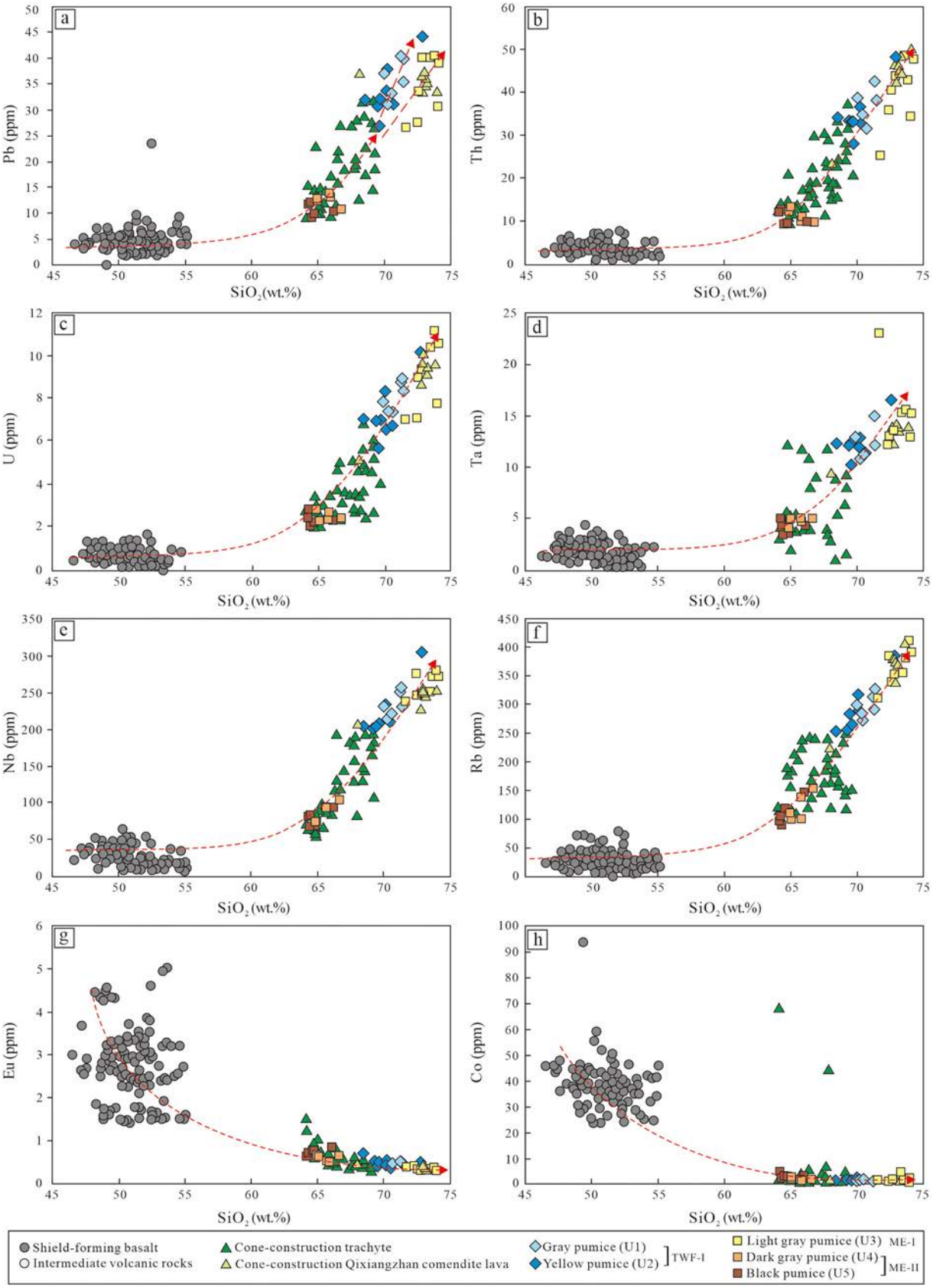

Fig. 6. Selected trace element variation diagrams. (a) Pb (ppm) versus SiO_2 (wt.%). (b) Th (ppm) versus SiO_2 (wt.%). (c) U (ppm) versus SiO_2 (wt.%). (d) Ta (ppm) versus SiO_2 (wt.%). (e) Nb (ppm) versus SiO_2 (wt.%). (f) Rb (ppm) versus SiO_2 (wt.%). (g) Eu (ppm) versus SiO_2 (wt.%). (h) Co (ppm) versus SiO_2 (wt.%). The geochemical data of the shield-forming basalts and intermediate volcanic rocks and the cone-construction trachyte and QXZ comenditic lava of the Tianchi volcano are from Liu et al. (2015) and Zhang et al. (2018).

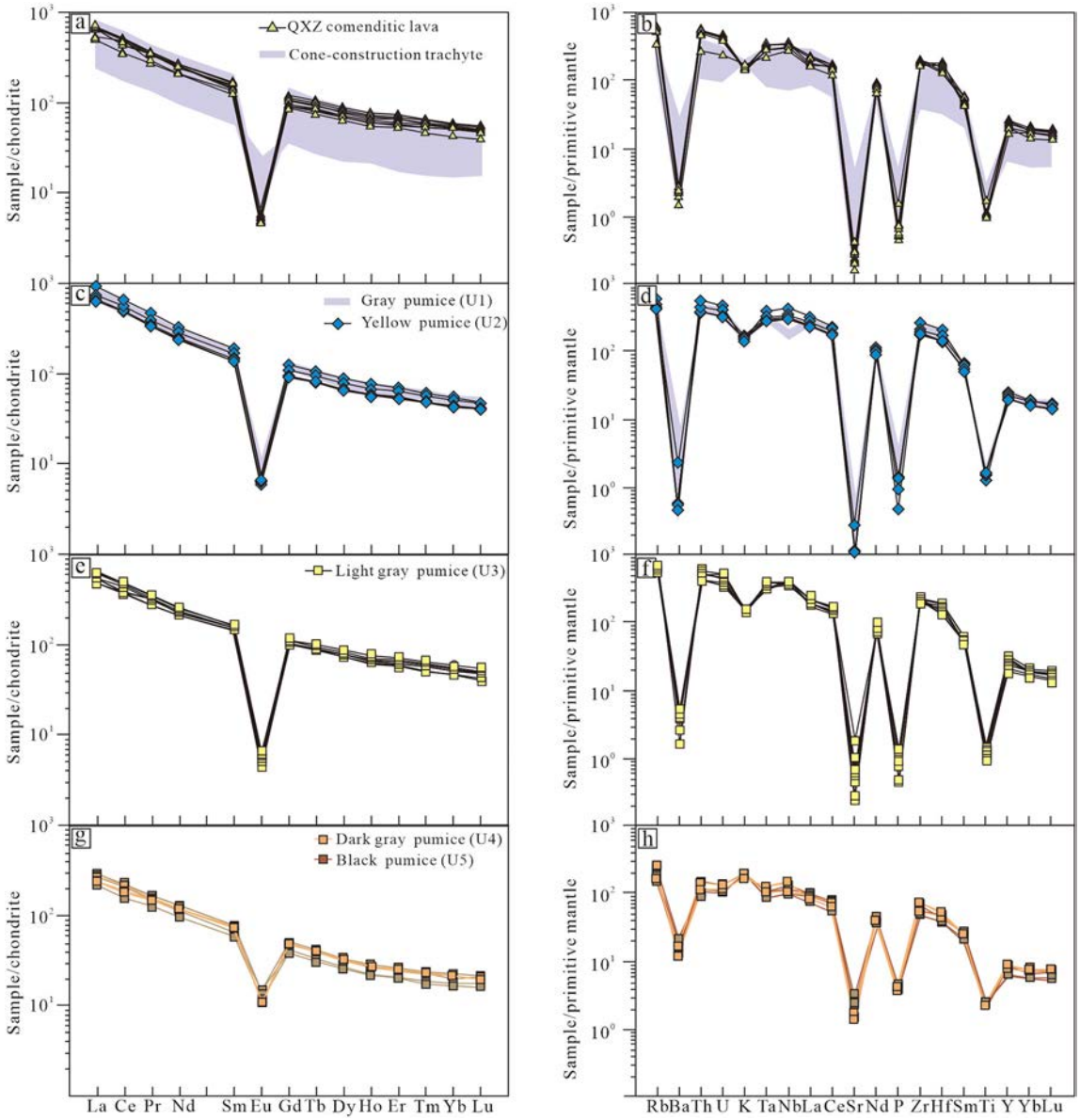

Fig. 7. Chondrite-normalized REE patterns (left column) and primitive mantle-normalized diagrams for volcanic rocks of the cone-construction stage and caldera-forming stage of Changbaishan. The data for the cone-construction trachyte and QXZ comenditic lava of are from Liu et al. (2015) and Zhang et al. (2018).

Based on these calculations, the depth of the magma chamber for ME-II was in the range of 2.5–3.3 km. This depth range overlaps with the magma storage depth of ME-I. Therefore, we speculate that the magma of ME-I and ME-II are most likely stored in the same shallow magma chamber (this will be analyzed in detail later in this article). The QXZ comenditic lava flow, which was the last eruption of the cone-construction stage, is the key to link the caldera-forming stage to the cone-construction stage. Andreeva et al. (2018) calculated the magma storage depth of QXZ comenditic lava to be 5–7 km, which is consistent with the small low-resistance anomaly in the lower part of Changbaishan volcano at approximately 5 km presented in Stone (2011). From the low-resistance anomaly, we can predict that there may be residual magma in this 5–7 km magma chamber. From the above discussion, at least two shallow magma chambers at different depths are assumed to exist in the upper crust of the caldera-forming stage of Changbaishan volcano.

A low-velocity anomaly recently found by Zhu et al. (2019) and a low density, sill-like body detected by Choi et al. (2013) from gravity data suggest that there exists a large magma chamber (approximately 8–15 km) in the mid curst. We conclude that the magma storage depth of the cone-construction trachytes is at approximately 8–15 km (Li et al., 2004; Guo et al., 2015, 2016; Liu et al., 2015). This depth corresponds to the upper-middle crust transition below Changbaishan (Choi et al., 2013). Therefore, the layering of the crust and possibly its rheology play a role in controlling the depth of magma storage zones below Changbaishan, a feature observed in other volcanic systems (Burov et al., 2003). However, the mid-crust magma chamber with a lateral extension of more than 100 km given by Zhu et al. (2019) according to the low-velocity anomaly is too large. There are more than 100 basic volcanic scoria cones that erupted in the cone-forming stage (Fig. 1) around the volcanic cone; e.g., the Laohudong basic scoria cone only 6.8 km from the eruption center (Fig. 14c) is located on the trachyte volcanic cone. These basic magmas that have erupted since 50 ka come from the lower crust-upper mantle basic magma chamber (Zheng et al., 1998; Wei et al., 2013; Park et al., 2016; Zhang et al., 2018). If there is a huge magma chamber with a diameter of more than 100 km storing

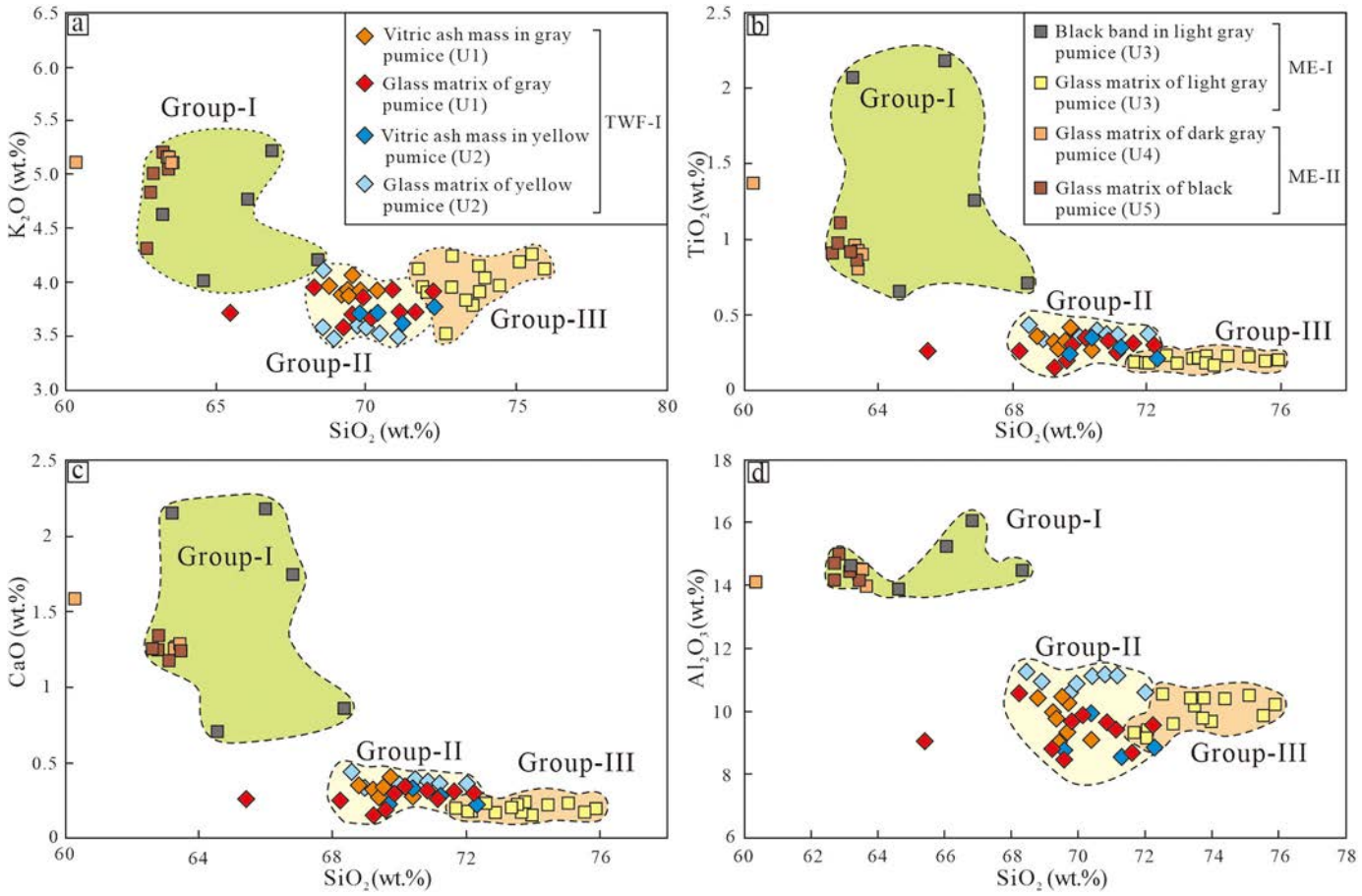

Fig. 8. Major element oxide ratios of glass matrixes and vitric ash masses. (a) K_2O (wt.%) versus SiO_2 (wt.%). (b) TiO_2 (wt.%) versus SiO_2 (wt.%). (c) CaO (wt.%) versus SiO_2 (wt.%). (d) Al_2O_3 (wt.%) versus SiO_2 (wt.%).

Table 2
Sr-Nd isotope data of pumices U1 to U5.

Unit	Sample No.	$^{87}Sr/^{86}Sr \pm 2\sigma m$	$^{143}Nd/^{144}Nd \pm 2\sigma m$
Gray pumices of U1	TWF-2b-2 W	0.709218 ± 0.000009	0.512588 ± 0.000007
	TWF-2a-2 W	0.708550 ± 0.000009	0.512591 ± 0.000008
	TWF-1a-2 W	0.709208 ± 0.000011	0.512620 ± 0.000014
	TWF-1b-2 W	0.708389 ± 0.000011	0.512575 ± 0.000012
	TWF-1c-2 W	0.707892 ± 0.000012	0.512588 ± 0.000016
	TWF-0-2 W	0.712231 ± 0.000009	0.512584 ± 0.000010
Yellow pumices of U2	TCB-7	0.708806 ± 0.000009	0.512604 ± 0.000011
	TCB-3a	0.708769 ± 0.000009	0.512607 ± 0.000009
	TCB-5Y	0.710594 ± 0.000009	0.512602 ± 0.000011
	TCB-3b	0.709195 ± 0.000010	0.512605 ± 0.000009
Light gray pumices of U3	TCN-6 W	0.708737 ± 0.000009	0.512593 ± 0.000007
	TCN-7 W	0.705643 ± 0.000006	0.512596 ± 0.000008
	TCN-1 W	0.706553 ± 0.000014	0.512594 ± 0.000008
	TCN-4 W	0.705533 ± 0.000014	0.512602 ± 0.000007
	TCB-8	0.705408 ± 0.000009	0.512597 ± 0.000012
Dark gray pumices of U4	TCB-2a	0.705090 ± 0.000007	0.512602 ± 0.000007
	TCB-1a	0.705105 ± 0.000007	0.512601 ± 0.000007
	TCB-1b	0.705124 ± 0.000010	0.512599 ± 0.000009
	TCB-2b	0.705112 ± 0.000009	0.512601 ± 0.000009
	TCB-2c	0.705099 ± 0.000009	0.512600 ± 0.000007
Black pumices of U5	TCB-6(1)	0.705130 ± 0.000009	0.512593 ± 0.000010
	TCB-6(2)	0.705098 ± 0.000010	0.512595 ± 0.000009
	TCB-6(3)	0.705054 ± 0.000011	0.512601 ± 0.000007
	TCB-6(4)	0.705079 ± 0.000010	0.512598 ± 0.000009
	TCB-6(5)	0.705086 ± 0.000009	0.512696 ± 0.000010

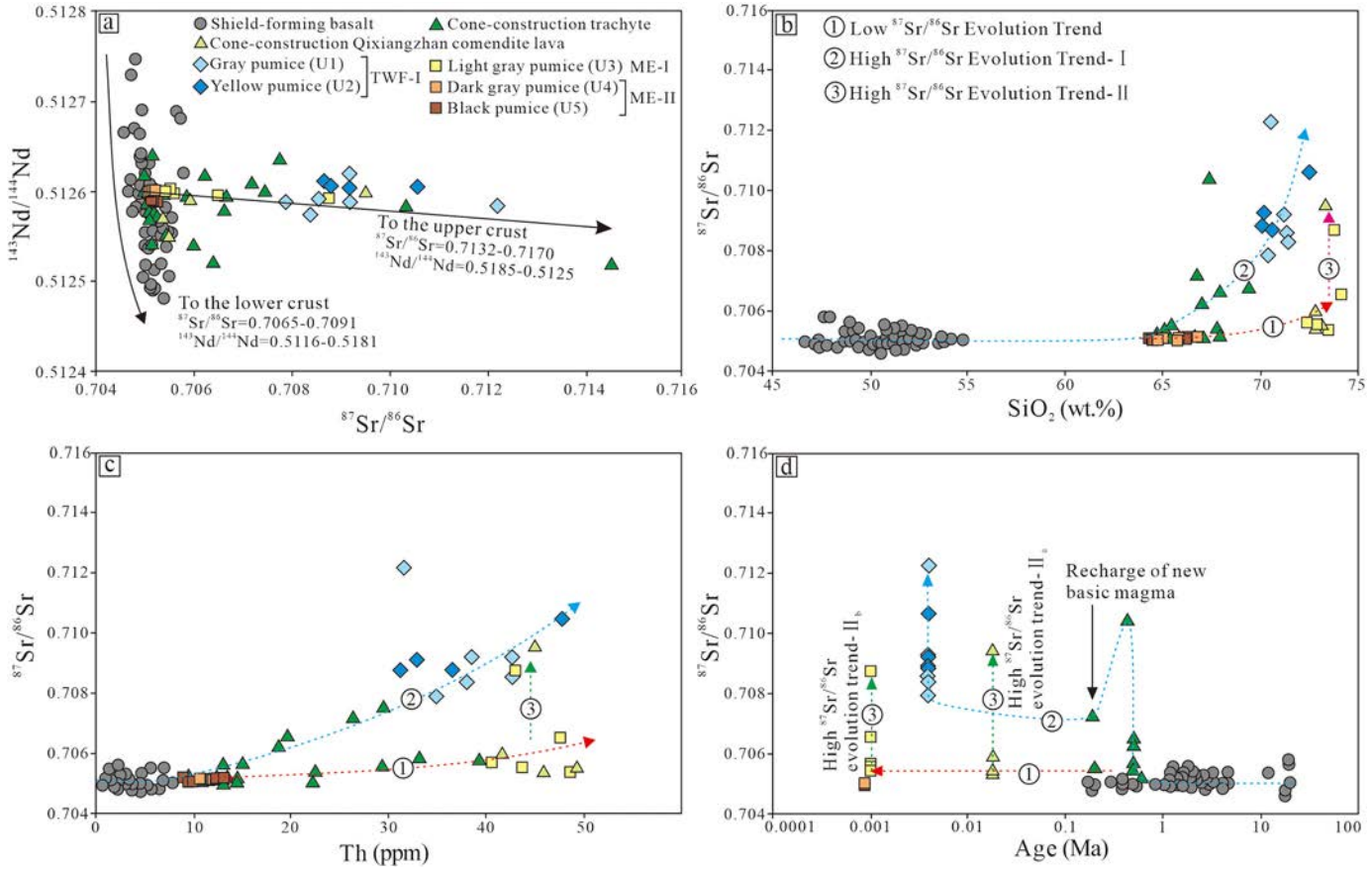

Fig. 9. (a) Sr-Nd isotope diagram of Changbaishan rocks, where data of the upper crust and lower crust are from Zhang et al. (2015). (b) $^{87}Sr/^{86}Sr$ versus SiO_2 (wt.%). (c) $^{87}Sr/^{86}Sr$ versus Th (ppm). (d) $^{87}Sr/^{86}Sr$ versus Age (Ma). The Sr-Nd isotopic dates of the shield-forming basalt and cone-construction trachyte and QXZ comenditic lava are from Guo et al. (2016) and Zhang et al. (2018). The isotopic age dates are from Liu and Wang (1982), Liu (1987), Yin et al. (2012), Xu et al. (2013), Singer et al. (2014), Yang et al. (2014) and Zhang et al. (2018).

Table 3
Summary of the mineral assemblage of pumices U1 to U5.

Unit	Feldspar					Clinopyroxene			Olivine		
	Af1		Af2	Af3	Pl1	Cpx1	Cpx2	Cpx3	Ol1	Ol2	
	Sh&	Sh#	Sa##	Sa##	Sh#	Sh&	Sh#	Sh#	R##	Sh&	Sr ##
Gray pumice of U1	−	++**	−	−	−	+**	−	−	+**	−	−
Yellow pumice of U2	−	++*	±	−	−	+*	−	−	±*	−	−
Light gray pumice of U3	+	−	−	−	−	±	−	−	−	−	−
Black band in light gray pumice of U3	−	−	+	−	−	−	−	−	−	−	+
Dark gray pumice of U4	−	−	+	±	±	−	±	±	−	±$	+
Black pumice of U5	−	−	+	±	−	−	±	±	−	−	±

Af1, alkali feldspar ($An_{<0.5}$, Or_{34-40} and Ab_{60-66}); Af2, alkali feldspar (An_{2-8}, Or_{38-48} and Ab_{48-57}); Af3, alkali feldspar (An_{16-21}, Or_{21-26}, Ab_{57-59}); Pl1, plagioclase (An_{38-57}, Or_{2-4}, Ab_{41-57}); Cpx1, clinopyroxene (En_{1-5}, Fs_{50-58}, Wo_{41-46}); Cpx2, clinopyroxene (En_{12-17}, Fs_{38-43}, Wo_{44-46}); Cpx3, clinopyroxene (En_{23-27}, Fs_{30-32}, Wo_{43-44}); Ol1, olivine ($Fo_{<1.5}$); Ol2, olivine (Fo_{13-16}). ++, abundant; +, a few; ±, rear and only present in few samples;-absent; ** all the crystals are crystal fragments in ash mass; * a part of crystal are crystal fragments in ash mass. Sa, subhedral to anhedral; Sh, subhedral; Sr, sub-round; R, round; ##, embayed dissolution texture; #, sieved dissolution; &, clean surface; $, wrapped in feldspar.

intermediate-acid magma in the middle crust beneath the Changbaishan caldera, it would be difficult for basic magma to pass through this mid crust magma chamber to arrive at the surface, which would prevent the formation of the observed widely distributed basic volcanic cinder cones (Hernando et al., 2016). Therefore, based on the distribution of the basic scoria cones, we believe that the lateral extension distance of the magma chamber in the middle crust of Changbaishan volcano does not exceed 10 km, and the vertical burial depth is approximately 10–15 km, which corresponds to the relatively strong part of low-velocity anomaly in the middle crust of Zhu et al. (2019). The excessive low-velocity anomaly may be related to limited observation conditions and too few seismic stations. Therefore, it is necessary to conduct intensive seismic array observation and 3D imaging research on Changbaishan Tianchi Volcano in the future.

The shield-forming basalts of Changbaishan evolved at depths ranging from 20 to 40 km in the lower crust and at Moho depth (Li et al., 2004; Guo et al., 2015). Basaltic eruptions from monogenic vents also occurred during the cone-construction stage from vents located around Changbaishan in the last 50 ka (Zheng et al., 1998; Wei et al., 2013; Park et al., 2016; Zhang et al., 2018). Considering that anomalies in seismic velocities and resistivity have been detected from 20 to 40 km in the lower crust and at the Moho (Hetland et al., 2004; Stone, 2011; Qiu

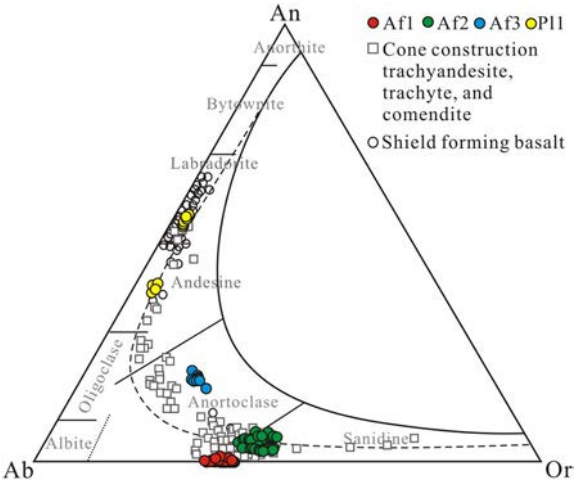

Fig. 10. Feldspar compositions for the analyzed samples of pumices U1 to U5. The data for the shield-forming basalts and cone-construction trachyandesite and trachyte of Changbaishan are from Li et al. (2004) and Chen et al. (2017). Af1: alkali feldspar ($An_{<0.5}$, Or_{34-40} and Ab_{60-66}); Af2: alkali feldspar (An_{2-8}, $Or_{38-48}$and Ab_{48-57}); Af3: alkali feldspar (An_{16-21}, Or_{21-26}, Ab_{57-59}); Pl1: plagioclase (An_{38-57}, Or_{2-4}, Ab_{41-57}).

et al., 2014; Kim et al., 2017; Wang and Chen, 2017), we suggest that the deeper magma feeding system of the volcano is located at the interface of the lower crust and the mantle-lower crust boundary. Geophysical observation results have also shown that the huge basic magma chamber has almost cooled in the local region with possibilities of only a high thermal state and partial melting (Kim et al., 2017), which corresponds with the fact that the amount of basic magma eruption decreased on a large scale in the manifestation of many small-scale basic scoria cone eruptions after the Changbaishan volcano entered the cone-forming and caldera eruption stages.

Based on the above discussed data, we deduce that the plumbing system of Changbaishan consists of (a) vertically extensive multiple reservoirs affecting the whole crustal volume and (b) magma chambers of the caldera-forming stage located at upper crustal depths of 0.5–3.5 km and at 10–15 km depths of the middle-lower crustal interface (Fig. 14c). The deeper storage zone of the less evolved magmas extends from the mantle-crust transition to the lower crust (Fig. 14c).

5.2. Magma evolution processes of the caldera-forming stage

Previous studies on the rocks of the three stage of activity of the Changbaishan volcano show evidence of an evolution trend from basalts to comendites related to fractional crystallization processes (Li et al., 2004; Andreeva et al., 2014; Liu et al., 2015; Pan et al., 2017a, 2017b; Zhang et al., 2018). The geochemical data collected in this study confirm an evolution by prevailing crystal fractionation from the cone-construction trachyandesites and trachytes to the caldera-forming trachytes and comendites (Figs. 5 and 6). The negative Eu anomalies and negative Ba, Sr, P, and Ti anomalies of the volcanic rocks in the cone-construction stage and caldera-forming stage imply the fractionation of plagioclase, pyroxene, and Fe-Ti oxides (Fig. 7). Minor crustal assimilation and mingling processes are also operating during the caldera-forming stage. However, the degree of fractionation of the studied products appears unrelated to the time of the eruptions and cannot be explained by the simple emptying of a single, zoned magma chamber. According to the results of the previously discussed geobarometric data and available geophysical data, the Changbaishan caldera is characterized by a complex plumbing system with multiple magma reservoirs located at different depths and where different magma batches may evolve and possibly mingle during the eruptions. The trachytic magma of the cone-construction stage is characterized by two main $^{87}Sr/^{86}Sr$ trends (Fig. 9b–d) that indicate different degrees of assimilation of upper crust material. The higher $^{87}Sr/^{86}Sr$ values may indicate the early emplacement of trachytic magma during the cone-construction stage (Fig. 9b–d). In this stage, the magma may assimilate high-$^{87}Sr/^{86}Sr$ country rocks. We call this magma chamber MCMC-I (10–15 km depth). After the early eruptions, the proportion of melt in MCMC-I gradually decreases, and a prevailing crystal mush remains. In the later cone-construction stage, new trachytic magma is injected into this residual mush, but this new magma is less able to assimilate crustal material because of the residual, crystal mush aureole isolates the reservoir from the country rocks (Guo et al., 2016). This process could explain the low-$^{87}Sr/^{86}Sr$ trend of the cone-construction stage of trachytes in Fig. 9b and c. We call this refilled magma chamber in the middle crust MCMC-II (10–15 km depth). The above-described picture well fits recent representations of crystal-poor melt segregation processes from crystal mushy reservoirs (Holness, 2018). This model invokes the rejuvenation of the magmatic system by replenishment processes, a mechanism fully compatible with the above-discussed evolution of the cone-construction stage at Changbaishan. In this picture, our geochemical and $^{87}Sr/^{86}Sr$ data for pumices U1 to U5 and the QXZ comenditic lava indicate that the origin of the magma in the caldera-forming stage (including the QXZ comenditic lava of the last cone-construction eruption) was inherited and evolved from the parental magmas in MCMC-I and MCMC-II of the cone-construction stage (Fig. 15a).

5.2.1. TWF eruption

Data from Figs. 5 and 9 suggest that the magma of the TWF eruption evolved from the residual melt of the early, high-$^{87}Sr/^{86}Sr$ trachytic magma from the cone-construction stage in MCMC-I (Fig. 15a). The small volume of the TWF eruption (Wei et al., 2013; Sun et al., 2017) also suggests that the TWF magma possibly derives from the emptying of a residual reservoir. Our calculation on the magma storage depth for the TWF eruption does not yield a reliable result using a clinopyroxene-liquid equilibrium because the iron-rich hedenbergite in gray and yellow pumices U1 and U2 is unsuitable in the calibration of the clinopyroxene-glass geothermometer (Zou et al., 2014). Although we do not know the exact magma storage depth for the TWF eruption (further research on pressure calculations using geobarometry from volatile saturation in melt inclusions is needed to determine the depth of the TWF reservoir), considering these limits and the available geochemical and isotopic data, we suggest that the TWF magma is associated with MCMC-I (Fig. 15a).

5.2.2. ME-I eruption

In Fig. 5d, the gray and yellow pumices of the TWF eruption and the light gray pumice of the ME-I eruption show separate evolution trends departing from the cone-construction trachytes. The comendites of ME-I cannot be related to a simple evolution from the TWF trachytes. In Fig. 9b–d, the light gray pumice of ME-I is located at the end of the low-$^{87}Sr/^{86}Sr$ trend. This result suggests that ME-I originated from the evolution of the later recharged trachytic magma with low-$^{87}Sr/^{86}Sr$ during the cone-construction stage in MCMC-II (Fig. 15a and b). Based on the analysis in Section 5.1—i.e., the depth of magma storage zones located in the upper crust—we argue that the low-$^{87}Sr/^{86}S$ trachytic magma in MCMC-II moved upward and evolved into a shallower magma chamber. We name this shallow magma chamber ME-I SMC-I (0.5–3.5 km depth) (Fig. 15a and b). In Fig. 9b–d, the light gray pumice of ME-I shows a nearly vertical sub-trend to high $^{87}Sr/^{86}Sr$. This may reflect the contamination and assimilation of country rocks in the SMC-I after the low-$^{87}Sr/^{86}Sr$ magma lefts MCMC-II (Fig. 15a and b).

A question that arises from Fig. 9b and c is whether the similar evolutionary trends of ME-I magma and QXZ magma indicate a relationship between them. Like ME-I magma, QXZ magma belongs to the low-$^{87}Sr/^{86}Sr$ trend, suggesting that it also formed by the evolution of the low-$^{87}Sr/^{86}Sr$ trachytic magma, probably in MCMC-II. The two

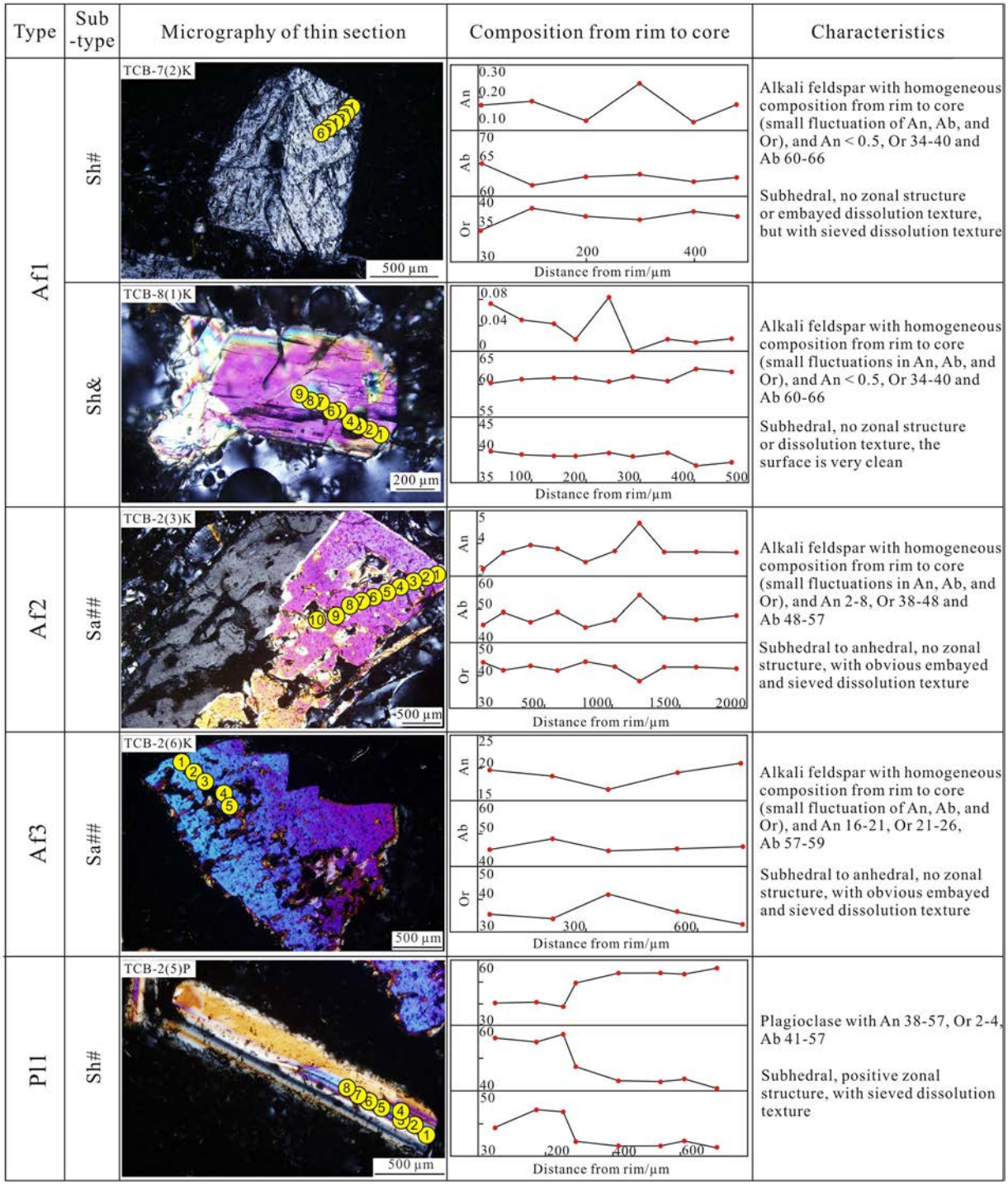

Fig. 11. Typical images and compositions of the four types of feldspars in pumices U1 to U5. Se: subhedral; Sa: subhedral to anhedral; ##: embayed dissolution texture; #: sieved dissolution; &: clean surface.

separated vertical sub-trends to high $^{87}Sr/^{86}Sr$ of the two magmas probably represent two independent low-$^{87}Sr/^{86}Sr$ magma rising events from MCMC-II (Fig. 9d). In addition, the magma storage depth of the QXZ comenditic lava—i.e., 5–7 km—is different from the depth inferred for the magma reservoir of ME-I—i.e., 0.5–3.5 km. These results prove that (a) the acidic magma of the QXZ eruption and ME-I, which evolved from the same parent melt, probably comes from two distinct shallow magma reservoirs and (b) the magma of ME-I does not represent the residual magma of the QXZ eruption.

5.2.3. ME-II eruption

The products of the latest caldera-forming event at Changbaishan have the lowest degree of evolution of the caldera-forming and cone-construction stages (Fig. 5). In the $^{87}Sr/^{86}Sr$ vs SiO_2 and $^{87}Sr/^{86}Sr$ vs Th diagrams (Fig. 9b and c), these pumices are located near the intersection point of the high-$^{87}Sr/^{86}Sr$ and low-$^{87}Sr/^{86}Sr$ trends. In the chondrite-normalized REE and primitive mantle-normalized incompatible element diagrams (Fig. 7), pumices U4 and U5 have the lowest negative Eu, Sr, P, and Ti anomalies of the rocks of the cone-construction stage

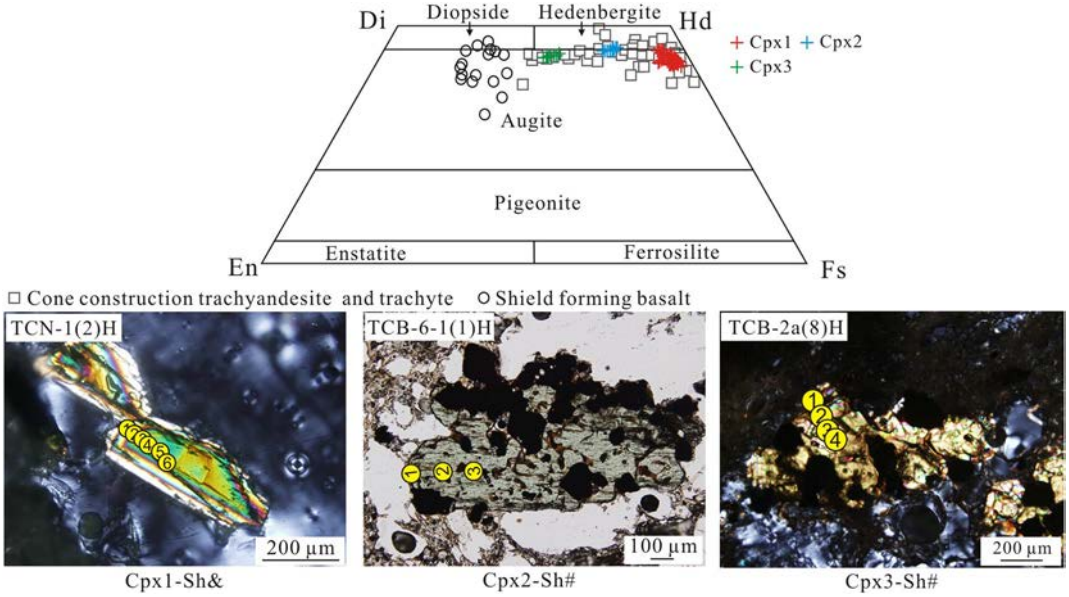

Fig. 12. Pyroxene compositions and typical images of the analyzed samples of pumices U1 to U5. The data for the shield-forming basalts and cone-construction trachyandesite and trachyte are from Li et al. (2004) and Chen et al. (2017). Cpx1: clinopyroxene (En_{1-5}, Fs_{50-58}, Wo_{41-46}); Cpx2: clinopyroxene (En_{12-17}, Fs_{38-43}, Wo_{44-46}); Cpx3: clinopyroxene (En_{23-27}, Fs_{30-32}, Wo_{43-44}).

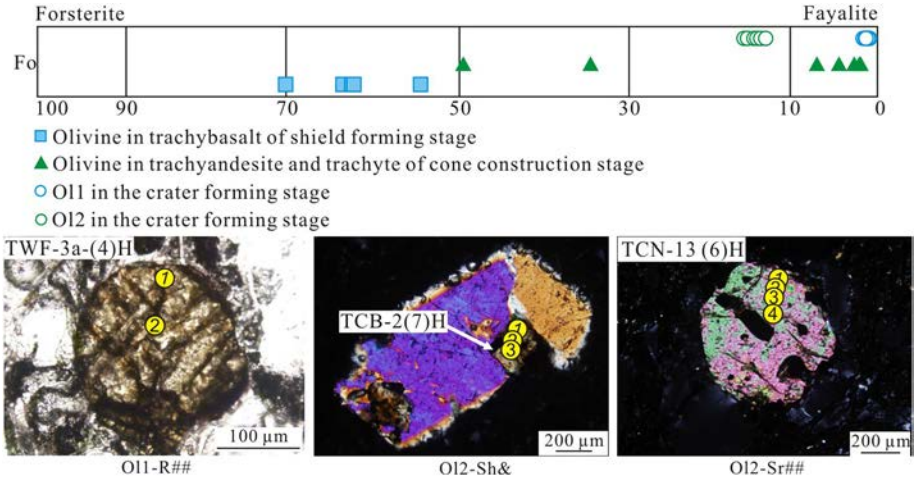

Fig. 13. Olivine composition and typical images for the analyzed samples of pumices U1 to U5. The data for the shield-forming basalt and cone-construction trachyandesite and trachyte of Changbaishan are from Li et al. (2004) and Chen et al. (2017). Sr: subrounded; R: rounded.

and the caldera-forming stage. The mineral assemblage of pumices U4 and U5 consists of Af2, Af3 and Pl1 feldspar, Cpx2 and Cpx3 clinopyroxene, and Ol2 olivine (Table 3). This mineral assemblage mainly developed in the early evolution stage of the trachytic magma during the cone-construction stage in the mid-crust (Li et al., 2004; Chen et al., 2017). The lower degree of evolution of the ME-II products with respect to the previous cone-construction stage and ME-I suggests that the ME-II magma probable formed by the injection of new trachytic magma into the mid-crust in the late caldera-forming stage (Fig. 15b). A question is whether the new ME-II magma was injected into an existing magma chamber or formed a new reservoir in the mid-crust. When the ME-II magma was injected, all residual magmas in MCMC-I and MCMC-II were in the late evolution stage (Figs. 5 and 6). The typical mineral assemblage of the later evolution stage of the trachyte and acidic magmas mainly consists of Af1, Cpx1, and Ol1 (with minor Af2 in the trachyte) (Fig. 5). If the ME-II magma was injected into an existing magma chamber, the ME-II magma should include minerals such as Af1, Cpx1, and Ol1. However, the mineral assemblage of ME-II does not have these typical minerals of the later evolution stage (Table 3). Therefore, we argue that the ME-II magma was injected into the mid-crust, did not mingle with older magma, and formed a new reservoir (MCMC-III, 10–15 km depth) (Fig. 15b).

According to the discussion in Section 5.1, we can state that the magma storage depth of the ME-II eruption is 2.5–3.3 km, indicating that the ME-II magma in the MCMC-III magma chamber moved upward and was stored in a shallow upper crust magma chamber before the ME-II eruption, and that the clinopyroxene and the melt are rebalanced after this shallow depth storage period. The TAS diagram (Fig. 3) and Hark diagram (Figs. 5 and 6) indicate that the dark gray pumice U4 that was erupted first has a slightly higher degree of evolution than the black pumice U5 that was erupted later, indicating that the ME-II magma has indeed experienced a short period of evolution in the shallow magma chamber. The magma composition in the magma chamber has a certain compositional differentiation in the vertical dimension,

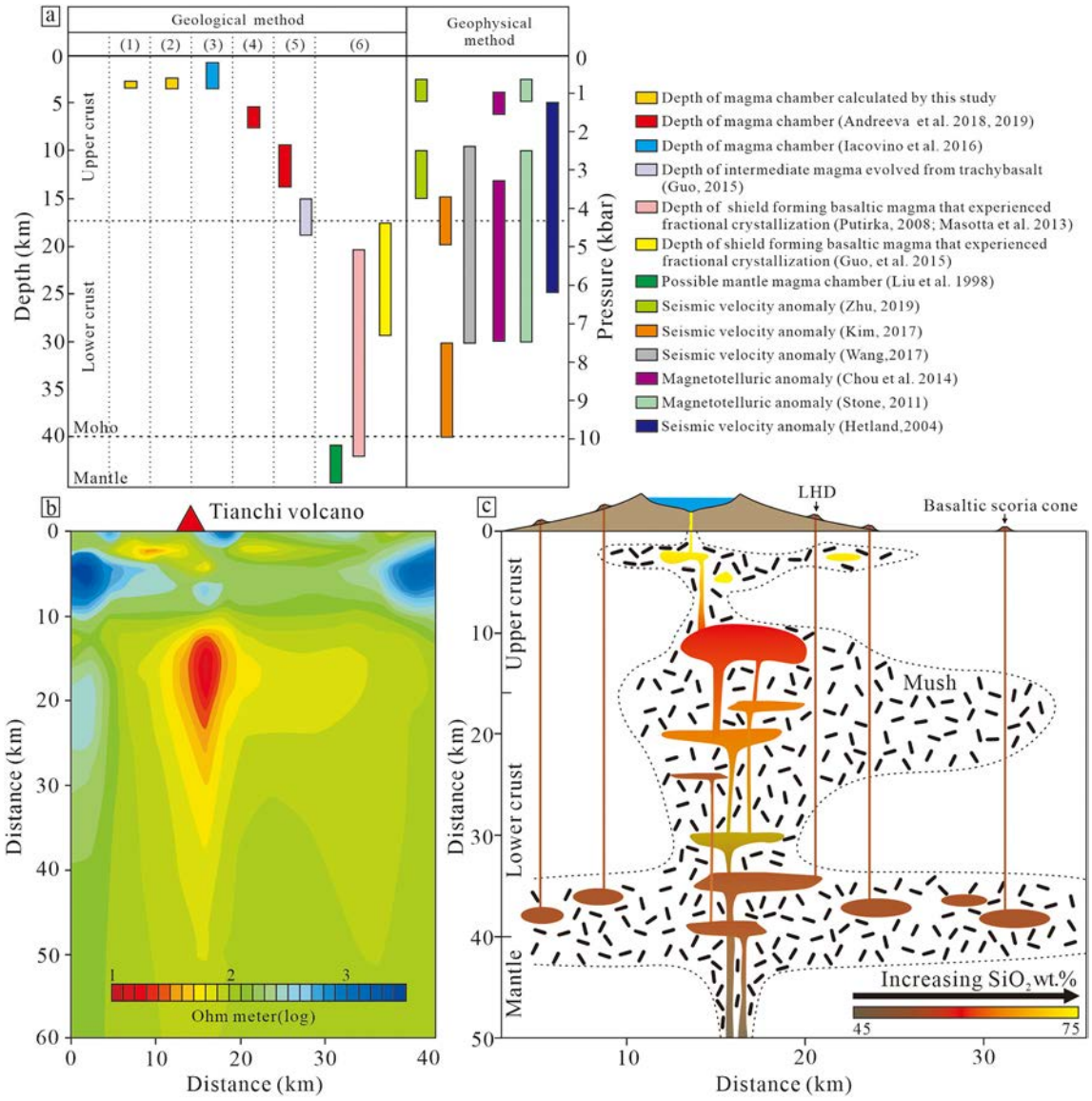

Fig. 14. (a) Depths of magma storage beneath Changbaishan estimated by geological and geophysical methods. (b) Crustal electric conductivity profile revealed by magnetotelluric data (Stone, 2011). (c) Probable crustal magma system of the caldera-forming stage. (1) Black pumice in U5; (2) dark gray pumice in U4; (3) light gray pumice in U3; (4) QXZ comenditic lava; (5) cone-construction trachyte; (6) shield-forming trachybasalt.

Table 4
Pressure and temperature estimation using clinopyroxene-liquid equilibria geobarometer.

Sample	Point	Distance from rim/μm	Phase	K_2O	FeO	MnO	TiO_2	Cr_2O_3	SiO_2	Al_2O_3	Na_2O	P_2O_5	MgO	CaO	NiO	Total	T(°C)	P(kbar)	K_D
Black pumice of U5																			
TCB-6-1(1)H	1	20	Cpx	0.01	22.11	0.74	0.57	0.00	49.36	0.68	0.47	0.05	5.18	20.23	0.01	99.41	899	0.7	0.14
			Glass	4.95	5.07	0.13	0.53	0.02	63.06	14.41	3.46	0.02	0.17	1.25	0.01	93.08			
TCB-6-1(2)H	1	20	Cpx	0.00	22.13	0.73	0.55	0.00	49.41	0.65	0.42	0.04	5.21	20.25	0.00	99.39	899	0.7	0.14
			Glass	4.95	5.07	0.13	0.53	0.02	63.06	14.41	3.46	0.02	0.17	1.25	0.01	93.08			
TCB-6-1(3)H	1	20	Cpx	0.01	22.17	0.76	0.59	0.00	49.35	0.66	0.43	0.05	5.09	20.31	0.00	99.42	899	0.7	0.15
			Glass	4.95	5.07	0.13	0.53	0.02	63.06	14.41	3.46	0.02	0.17	1.25	0.01	93.08			
TCB-6-2(1)H	1	20	Cpx	0.00	22.15	0.76	0.58	0.00	49.29	0.70	0.45	0.00	5.21	20.20	0.00	99.35	901	0.7	0.15
			Glass	4.86	5.05	0.12	0.56	0.02	62.85	14.50	3.16	0.02	0.18	1.25	0.00	92.57			
TCB-6-2(2)H	1	20	Cpx	0.00	22.21	0.80	0.58	0.00	49.28	0.65	0.44	0.00	5.04	20.20	0.00	99.20	899	0.8	0.16
			Glass	4.86	5.05	0.12	0.56	0.02	62.85	14.50	3.16	0.02	0.18	1.25	0.00	92.57			
Dark gray pumice of U4																			
TCB-2a (1)H	1	20	Cpx	0.00	22.08	0.75	0.58	0.00	49.34	0.69	0.47	0.00	5.19	20.26	0.00	99.42	898	0.6	0.13
			Glass	5.13	5.10	0.13	0.48	0.01	63.38	14.27	3.91	0.01	0.15	1.26	0.01	93.83			
TCB-2a (2)H	1	20	Cpx	0.00	22.23	0.82	0.63	0.04	49.35	0.71	0.42	0.02	5.09	20.07	0.00	99.38	896	0.7	0.13
			Glass	5.13	5.10	0.13	0.48	0.01	63.38	14.27	3.91	0.01	0.15	1.26	0.01	93.83			

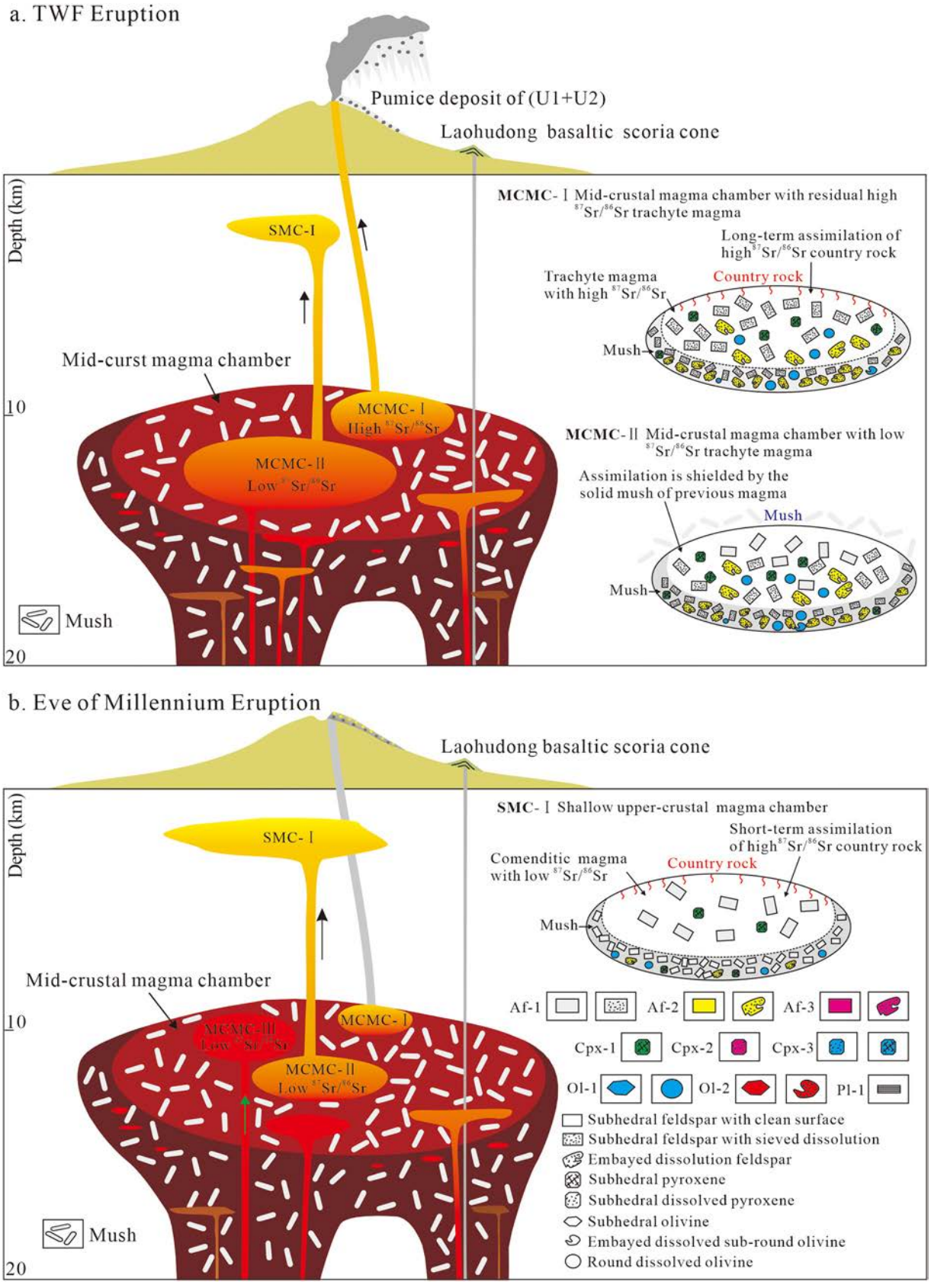

Fig. 15. Crustal magma chamber system and magma evolution process of the caldera-forming stage at Changbaishan. The mineral assemblages of MCMC-I and MCMC-II are from Li et al. (2004) and Chen et al. (2017).

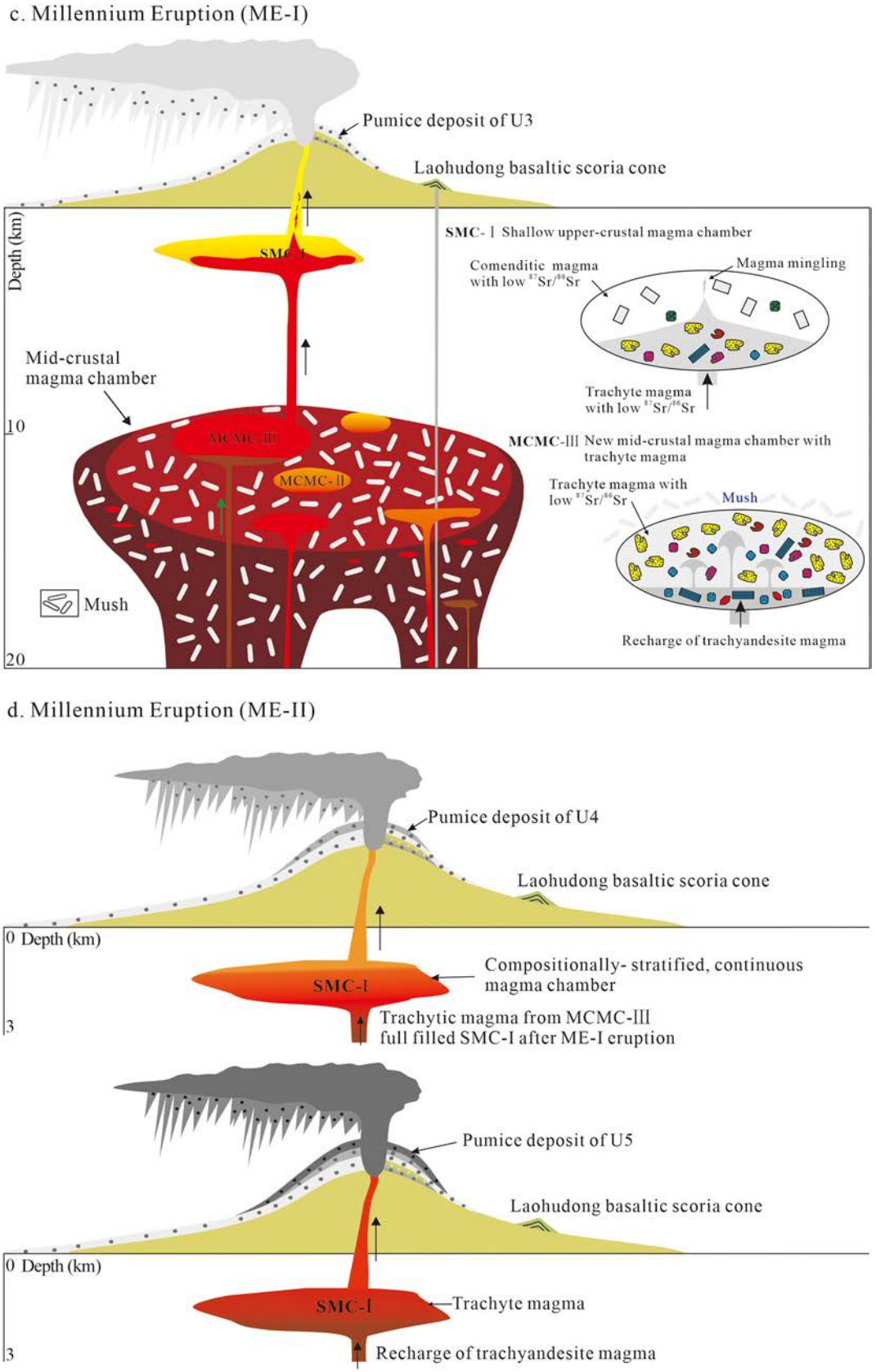

Fig. 15 (*continued*).

and this shallow magma chamber belongs to the compositionally stratified magma chamber.

5.3. Magma mingling

Based on the observation that the black bands in the gray pumice of ME-I have compositions and a mineral assemblage similar to that of the black pumices of ME-II (e.g., Fig. 8, Table 3), Pan et al. (2017a,b) demonstrated that the black bands in the light gray pumice of ME-I formed by mixing of the comenditic magma (ME-I) and trachytic magma (ME-II) during ME. In our samples, all phenocrysts in the gray pumice of ME-I show clean surfaces without dissolution textures. The clean surfaces of minerals can reflect stable temperature and pressure conditions in the magma chamber. Therefore, before the ME, the ME-I magma in the shallow magma chamber may have maintained nearly constant temperature and pressure for a long time without mixing—i.e., thermal disequilibrium (Sparks and Marshall, 1986). In addition, there are almost no phenocrysts in the light gray pumice (except in the black bands) with composition similar to that of the phenocrysts in the dark gray and black pumices. These observations indicate that the mixing processes occurred easily during the eruption and not before. Considering the temporal relationship between the magmas of ME-II and ME-I, the ME eruption was triggered probably by the sudden injection of a trachytic magma (Fig. 15c). There are two possibilities for a such trigger mechanism. One possibility is that the trachytic magma rose from MCMC-III and formed another shallow magma chamber, then the ME-II and the ME-I magma chambers were directly connected. A typical example is the 1815 CE Tambora (Indonesia) eruption in the Heise volcanic field, and those in the Snake River Plain–Yellowstone Plateau (SRP-YP) volcanic province in eastern Idaho (Wotzlaw et al., 2014). The other possibility is that the trachytic magma of MCMC-III in the mid-crust rapidly rose and mixed with the acidic magma of ME-I, thus triggering ME. The first possibility is difficult to reconcile with the magma storage times, and our $^{87}Sr/^{86}Sr$ data do not evidence significant assimilation of upper crustal material and, as a consequence, long residence times. In fact, much time is required to form a new magma chamber (Townsend and Huber, 2020). Chronological studies by various methods such as U-series zircon dating, $^{40}Ar/^{39}Ar$ dating and ^{14}C dating show that (in Table 5) after ME-I magma rises from the middle crust magma chamber, it takes 10–11 ka to form the SMC-I shallow crust magma chamber; however, the residence time of ME-II in the shallow crust is much shorter than this time (Zou et al., 2010, 2014; Xu et al., 2013; Yang et al., 2014; Ramos et al., 2016). Moreover, all minerals in ME-II are dissolved. The lack of newly formed euhedral undissolved mineral also suggests the short storage and evolution time for ME-II magma. Therefore, we prefer the latter interpretation and favor the second hypothesis (Fig. 15c). During the ME-I eruption, suction led to the mixture of ME-II magma in the bottom of the magma chamber with the upper ME-I magma (Kaneko et al., 2007). We underline that magma mixing is considered an important triggering mechanism of volcanic eruptions (De Silva et al., 2008), and the last stages of activity at Changbaishan show that this mechanism operates.

After the ME-I magma was emptied, the SMC-I magma chamber was filled with the ME-II magma. The eruption was suspended, and after a short period of evolution, a compositionally stratified, continuous magma chamber was formed, and then the ME-II eruption occurred again, forming accumulation of pumices U4 and U5 (Fig. 15d).

5.4. Basaltic magma recharge

Some typical textural and mineralogical features can be used to identify basaltic magma recharge, including lavas with euhedral to rounded sieved feldspars, some with clear (no sieved) rims of more calcic or sodic composition, feldspars with reverse zoning, and biotite with replacement by anhydrous minerals (Hernando et al., 2016). In this study, we did not find minerals with these typical textures in the pumices of the caldera-forming stage. Data from Figs. 10 and 12 clearly show no overlaps between the crystal compositions of the shield-forming stage and the caldera-forming stage. Hence, there is no clear evidence of large-scale basaltic magma recharge occurring in the caldera-forming stage, at least in the reservoirs of the middle-upper crust.

In the dark gray and black pumices of the ME-II eruption, we find two types of pyroxene, Cpx2 and Cpx3, and three types of feldspar, Pl-1, Af-2 and Af-3. Pl-1 and Cpx3 are considered to have formed in intermediate magmas with a lower degree of evolution than the magma of ME-II according to the mineralogical analysis for the cone-construction stage by Li et al. (2004) and Chen et al. (2017) (Figs. 10 and 12). In addition, almost all minerals show dissolution textures in the pumices of ME-II. Therefore, we argue that intermediate magma was persistently recharged into the trachytic magma of ME-II and may have evolved from basalts in the lower crust and/or at the Moho depth (Fig. 15 c and d).

The results of our study show that the plumbing of the Changbaishan caldera stage is partly inherited from that responsible for the cone-construction, pre-caldera stage and consists of multiple reservoirs located at different depths. Fractionation and crustal assimilation processes operated in these reservoirs. The Changbaishan plumbing system affects the upper 10–15 km of the crust and is characterized by crystal mushy zones from which melts are extracted by magma replenishment. The triggering mechanism of the ME event was the arrival of fresh, trachytic magma entering a comenditic magma chamber. The multiple-level plumbing system of Changbaishan is similar to that proposed for other volcanoes including those of the Snake River Plain (US), Taupo, (New Zealand), Long Valley (US), and Cerro Galan (Argentina), where two or more vertically arranged magma reservoirs have been detected by geochemical or geophysical data (Cashman and Giordano, 2014). This storage configuration implies a rapid assembly of plumbing systems provided that the magma supply rate from depth is high. The monitoring signals possibly associated with eruptions from multi-level reservoirs are difficult to interpret because of the complex nature of such plumbing systems. Magma recharge episodes may destabilize a part of or the entire plumbing system, thus promoting eruptions of different sizes and eruptive styles. Therefore, a reference model for active calderas like that proposed here for Changbaishan is required to

Table 5
Geochronology of the recent eruptions of the Changbaishan Tianchi volcano.

Eruption	Dating method	Age	Geological connotation	Reference
QXZ Eruption	^{40}Ar-^{39}Ar dating	17.1 ± 0.9 ka	Eruption	Singer et al., 2014
TWF	^{40}Ar-^{39}Ar dating	4.2 ± 0.4 ka	Eruption	Yang et al., 2014
ME-I	^{40}Ar-^{39}Ar dating	1.24 ± 0.51 ka	Eruption	Yang et al., 2014
ME-I	^{14}C dating	946 ± 3 C.E.	Eruption	Xu et al., 2013
ME-I	U-series zircon dating	12.2 ± 1.7 ka	Magma chamber forming	Zou et al., 2010, 2014; Ramos et al., 2016
ME-II	U-series zircon dating	2.6 ± 1.8 ka	Magma chamber forming	Zou et al., 2014
ME-II	^{14}C dating	980 ± 65C.E.	Eruption	Yin et al., 2005

correctly interpret possible unrest episodes and possibly anticipate future volcanic eruptions.

6. Conclusions

The results of this study may be summarized in the following main points:

(1) The Changbaishan caldera-forming stage involved a complex plumbing system including shallow magma chambers at a depth of 0.5–3 km and a mid-crustal magma chamber at a depth of 10–15 km and at the upper-lower crust boundary, as well as some residual basic magma chambers at the crust-mantle boundary. Magma segregation processes of crystal poor melts from crystal mushy reservoirs were allowed by replenishment processes.
(2) The magmas of the TWF eruption and the ME-I eruption were inherited and evolved from the parental magma of the previous cone-construction stage. The ME-II event was triggered by a new arrival of trachytic magma.
(3) There is no clear evidence of large-scale basaltic magma recharge occurring in the caldera-forming stage. Intermediate magma recharged the ME-II. The mixture of the trachytic magma of ME-II and acidic magma of ME-I occurred in the conduit during the ME eruption. The ME eruption was most likely triggered by the sudden arrival of ME-II trachytes.
(4) The magma of the first (TWF) eruption of the caldera-forming stage and the magma of the last eruption of the cone-construction stage (QXZ eruption) have no relationships and come from two distinct reservoirs. The magma of ME-I was not inherited from the residual magma of the early QXZ eruption and evolved in a shallower reservoir.

The availability of a reference model at Changbaishan and other calderas allows us to constrain the interpretation of data from the monitoring of deformation, earthquakes, and gas geochemistry. These data may help in detecting the possible arrival of new magma and its storage depth and in investigating the processes operating in reservoirs located at different depths.

Declaration of competing interest

The authors declare that they have no known competing financial interests or personal relationships that could have appeared to influence the work reported in this paper.

Acknowledgments

This study was funded by the National Natural Science Foundation of China under Grant Nos. 41972313 and 41790453 and by the Engineering Research Center of Geothermal Resources Development Technology and Equipment, Ministry of Education, Jilin University, China.

Appendix A. Supplementary data

Supplementary data to this article can be found online at https://doi.org/10.1016/j.gsf.2021.101171.

References

Andreeva, O.A., Yarmolyuk, V.V., Andreeva, I.A., Ji, J.Q., Li, W.R., 2014. The composition and sources of magmas of Changbaishan Tianchi Volcano (China–North Korea). Dokl. Earth Sci. 456, 572–578.
Andreeva, O.A., Yarmolyuk, V.V., Andreeva, I.A., Borisovskiy, S.E., 2018. Magmatic evolution of Changbaishan Tianchi Volcano, China-North Korea: evidence from mineral-hosted melt and fluid inclusions. Petrology 26, 515–545.
Burov, E., Jaupart, C., Guillou-Frottier, L., 2003. Ascent and emplacement of buoyant magma bodies in brittle–ductile upper crust. J. Geophys. Res.-Sol. Ea. 108, 2177.
Cashman, K.V., Giordano, G., 2014. Calderas and magma reservoirs. J. Volcanol. Geotherm. Res. 288, 28–45.
Cashman, K.V., Sparks, R.S.J., Blundy, J.D., 2017. Vertically extensive and unstable magmatic systems: a unified view of igneous processes. Science 355, eaag3055.
Chen, F., Hegner, E., Todt, W., 2000. Zircon ages and Nd isotopic and chemical compositions of orthogneisses from the Black Forest, Germany: evidence for a Cambrian magmatic arc. Int. J. Earth Sci. 88, 791–802.
Chen, X.W., Wei, H.Q., Yang, L.F., Chen, Z.Q., 2017. Petrological and mineralogical characteristics of Tianchi Volcanoe, Changbai Mountain: Implications for crystallization differentiation and magma mixing. Acta Geosci. Sin. 38, 177–192.
Choi, S., Oh, C.W., Götze, H.J., 2013. Three-dimensional density modeling of the EGM2008 gravity field over the Mount Paekdu volcanic area. J. Geophys. Res.-Sol. Ea. 118, 3820–3836.
Costa, A.J., Suzuki, Y., Koyaguchi, T., 2018. Understanding the plume dynamics of explosive super-eruptions. Nat. Commun. 9, 654.
De Silva, S., Salas, G., Schubring, S., 2008. Triggering explosive eruptions-the case for silicic magma recharge at Huaynaputina, southern Peru. Geology 36, 387.
Dostal, J., Dupuy, C., Zhai, M., Zhi, X., 1988. Geochemistry and origin of Pliocene alkali basaltic lavas from Anhui-Jiangsu, Eastern China. Geochem. J. 22, 165–176.
Forni, F.W., Degruyter, O., Bachmann, G., De Astis, S., Mollo, S., 2018. Long-term magmatic evolution reveals the beginning of a new caldera cycle at Campi Flegrei. Sci. Adv. 4, eaat9401.
Geyer, A., Folch, A., Marti, J., 2006. Relationship between caldera collapse and magma chamber withdrawal: an experimental approach. J. Volcanol. Geotherm. Res. 157, 375–386.
Geyer, A., Alvarez-Valero, A.M., Gisbert, G., Aulinas, M., Hernandez-Barrena, D., Lobo, A., Marti, J., 2019. Deciphering the evolution of Deception Island's magmatic system. Sci. Rep. 9, 373.
Guo, Z.F., Liu, J.Q., Sui, S.Z., Liu, Q., He, H.Y., Ni, Y.Y., 2002. The mass estimation of volatile emission during 1199-1200 AD eruption of Baitoushan volcano and its significance. Sci. China Earth Sci. 45, 530–539.
Guo, Z.F., Liu, J.Q., Han, J.T., He, H.Y., Dai, G.L., You, H.T., 2006. Effect of gas emissions from Tianchi volcano (NE China) on environment and its potential volcanic hazards. Sci. China Earth Sci. 49, 304–310.
Guo, W.F., Liu, J.Q., Xu, W.G., Li, W., Lei, M., 2015. Reassessment of the magma system beneath Tianchi volcano, Changbaishan: phase equilibria constraints. Chin. Sci. Bull. 60, 3489–3500.
Guo, W.F., Liu, J.Q., Wu, C.L., Lei, M., Qin, H.P., Wang, N., Zhang, X., Cheng, H.J., Wang, Z., 2016. Petrogenesis of trachyte and the felsic magma system at Tianchi Volcano. Geol. Rev. 62, 617–630.
Hernando, I.R., Petrinovic, I.A., Llambías, E.J., D'Elia, L., González, P.D., Aragón, E., 2016. The role of magma mixing and mafic recharge in the evolution of a back-arc quaternary caldera: the case of Payún Matrú, Western Argentina. J. Volcanol. Geotherm. Res. 311, 150–169.
Hetland, E.A., Wu, F.T., Song, J.L., 2004. Crustal structure in the Changbaishan volcanic area, China, determined by modeling receiver functions. Tectonophysics 386, 157–175.
Holness, M.B., 2018. Melt segregation from silicic crystal mushes: a critical appraisal of possible mechanisms and their microstructural record. Contrib. Mineral. Petrol. 173, 48.
Horn, S., Schmincke, H.U., 2000. Volatile emission during the eruption of Baitoushan Volcano (China/North Korea) ca. 969 AD. Bull. Volcanol. 61, 537–555.
Iacovino, K., Kim, J.S., Sisson, T., Lowenstern, J., Ri, K.H., Jang, J.N., Song, K.H., Ham, S.H., Oppenheimer, C., Hammond, J.O.S., Donovan, A., Liu, K.W., Ryu, K.R., 2016. Quantifying gas emissions from the "Millennium Eruption" of Paektu volcano, Democratic People's Republic of Korea/China. Sci. Adv. 2, e1600913.
Irvine, T.N., Baragar, W.R.A., 1971. A guide to the chemical classification of the common volcanic rocks. Can. J. Earth Sci. 8, 523–548.
Jin, B.L., Zhang, X.Y., 1994. Researching Volcanic Geology in Mount Changbai. Northeast Korea Nationality Education Press, Yanbian.
Kaneko, K., Kamata, H., Koyaguchi, T., Yoshikawa, M., Furukawa, K., 2007. Repeated large-scale eruptions from a single compositionally stratified magma chamber: an example from Aso volcano, Southwest Japan. J. Volcanol. Geotherm. Res. 167, 160–180.
Kennedy, B.M., Holohan, E.P., Stix, J., Gravley, D.M., Davidson, J.R.J., Cole, J.W., 2018. Magma plumbing beneath collapse caldera volcanic systems. Earth-Sci. Rev. 177, 404–424.
Kern, A.K., Kovar-Eder, J., Stachura-Suchoples, K., Wang, W.M., Wang, P., 2016. Radiometric dating re-evaluating the paleoenvironment and paleoclimate around the Plio–Pleistocene boundary in NE China (Changbai Mountains). Rev. Palaeobot. Palynol. 224, 134–145.
Kim, S., Tkalčić, H., Rhie, J., 2017. Seismic constraints on magma evolution beneath Mount Baekdu (Changbai) volcano from transdimensional Bayesian inversion of ambient noise data. J. Geophys. Res.-Sol. Ea. 122, 5452–5473.
Kruger, W., Latypov, R., 2020. Fossilized solidifications fronts in the Bushveld complex argues for liquid-dominated magmatic systems. Nat. Commun. 11, 2909.
Le Bas, M.J., Le Maitre, R.W., Streckeison, A., Zanettin, B., 1986. A chemical classification of volcanic rocks based on the total alkali-silica diagram. J. Petrol. 27, 745–750.
Le Maitre, R., Bateman, P., Dudek, A., Keller, J., Lameyre, J., Le Bas, M., Sabine, P., Schmid, R., Sorensen, H., Streckeisen, A., Woolley, A., Zanettin, B., 1989. A Classification of Igneous Rocks and Glossary of Terms. Blackwell, Oxford.
Lei, J.S., Xie, F., Fan, Q.C., Santosh, M., 2013. Seismic imaging of the deep structure under the Chinese volcanoes: an overview. Phys. Earth Planet. Inter. 224, 104–123.
Li, N., Fan, Q.C., Sun, Q., Zhang, W.L., 2004. Magma evolution of Changbaishan Tianchi volcano: Evidences from the main phenocrystal minerals. Acta Petrol. Sin. 20, 575–582.

Liu, J.Q., 1987. Study on geochronology of the Cenozoic volcanic rocks in NE China. Acta Petrol. Sin. 4, 21–31 (in Chinese with English abstract).
Liu, J.Q., Wang, S.S., 1982. Changbaishan volcano and the age of Tianchi. Chin. Sci. Bull. 21, 1312–1315.
Liu, X., Xiang, T.Y., 1997. Cenozoic Volcanoes and Pyroclastic Deposits in Northeast China: Resources and Hazards. Jilin University Publishing House, Changchun (in Chinese).
Liu, R.X., Li, J.T., Wei, H.Q., Xu, D.M., Zheng, X.S., 1992. Volcano at Tianchi lake, Changbaishan Mt. a modern volcano with potential danger of eruption. Chin. J. Geophys. 35, 661–665 (in Chinese with English abstract).
Liu, G.M., Sun, H.Y., Guo, F., 2011. The newest monitoring information of Changbaishan volcano, NE China. Acta Petrol. Sin. 27, 2905–2911 (in Chinese with English abstract).
Liu, J.Q., Chen, S.S., Guo, Z.F., Guo, W.F., He, H.Y., You, H.T., Kim, H.M., Sung, G.H., Kim, H., 2015. Geological background and geodynamic mechanism of Mt. Changbai volcanoes on the China-Korea border. Lithos 236-237, 46–73.
Liu, G.M., Li, C.Y., Peng, Z.G., Li, X.M., Wu, J., 2017. Detecting remotely triggered microseismicity around Changbaishan volcano following nuclear explosions in North Korea and large distant earthquakes around the world. Geophys. Res. Lett. 44, 4829–4838.
Machida, H., Moriwaki, H., Zhao, D.C., 1990. The recent major eruption of Changbai volcano and its environmental effects. Geograph. Rep. Tokyo Metropolitan University 5, 1–20.
Mason, B.G., Pyle, D.M., Oppenheimer, C., 2004. The size and frequency of the largest explosive eruptions on Earth. Bull. Volcanol. 66, 735–748.
Masotta, M., Mollo, S., Freda, C., Gaeta, M., Moore, G., 2013. Clinopyroxene–liquid thermometers and barometers specific to alkaline differentiated magmas. Contrib. Mineral. Petrol. 166, 1545–1561.
Myers, M.L., Geist, D.J., Rowe, M.C., Harpp, K.S., Wallace, P.J., Dufek, J., 2014. Replenishment of volatile-rich mafic magma into a degassed chamber drives mixing and eruption of Tungurahua volcano. Bull. Volcanol. 76, 872.
Pan, B., de Silva, S.L., Xu, J.D., Chen, Z.Q., Miggins, D.P., Wei, H.Q., 2017a. The VEI-7 Millennium eruption, Changbaishan-Tianchi volcano, China/DPRK: New field, petrological, and chemical constraints on stratigraphy, volcanology, and magma dynamics. J. Volcanol. Geotherm. Res. 343, 45–59.
Pan, B., Fan, Q.C., Xu, J.D., Wu, C.Z., Chen, Z.Q., Guo, F., 2017b. Magmatic processes of the Millennium eruption at Changbaishan Tianchi volcano, China/North Korea. Acta Petrol. Sin. 33, 163–172 (in Chinese with English abstract).
Pan, B., de Silva, S.L., Xu, J.D., Liu, S.J., Xu, D., 2020. Late Pleistocene to present day eruptive history of the Changbaishan-Tianchi Volcano, China/DPRK: New field, geochronological and chemical constraints. J. Volcanol. Geotherm. Res. 399, 106870.
Papale, P., Marzocchi, W., 2019. Volcanic threats to global society. Science 363, 1275–1276.
Park, S.C., Kim, T.U., Cho, I.W., Kim, S.C., Kin, I.C., 2016. Scoriae magma evolution at Paekdu volcano, Democratic People's Republic of Korea. Acta Petrol. Sin. 32, 3214–3224 (in Chinese with English abstract).
Putirka, K.D., 2008. Thermometers and barometers for volcanic systems. Rev. Mineral. Geochem. 69, 61–120.
Putirka, K., Johnson, M., Kinzler, R., Longhi, J., Walker, D., 1996. Thermobarometry of mafic igneous rocks based on clinopyroxene-liquid equilibria, 0-30 kbar. Contrib. Mineral. Petrol. 123, 92–108.
Putirka, K.D., Mikaelian, H., Ryerson, F., Shaw, H., 2003. New clinopyroxene–liquid thermobarometers for mafic, evolved, and volatile-bearing lava compositions, with applications to lavas from Tibet and the Snake River Plain. Idaho. Am. Mineral. 88, 1542–1554.
Qiu, G.G., Fei, F.G., Fang, H., Du, B.R., Zhang, X.B., Zhang, P.H., Yuan, Y.Z., He, M.X., Bai, D.W., 2014. Analysis of magma chamber at the Tianchi volcano area in Changbai mountain. Chin. J. Geophys. 57, 3466–3477 (in Chinese with English abstract).
Ramos, F.C., Heizler, M.T., Buettner, J.E., Gill, J.B., Wei, H.Q., Dimond, C.A., Scott, S.R., 2016. U-series and $^{40}Ar/^{39}Ar$ ages of Holocene volcanic rocks at Changbaishan volcano, China. Geology 44, 511–514.
Singer, B.S., Jicha, B.R., He, H.Y., Zhu, R.X., 2014. Geomagnetic field excursion recorded 17 ka at Tianchi Volcano, China: New $^{40}Ar/^{39}Ar$ age and significance. Geophys. Res. Lett. 41, 2794–2802.
Sparks, R.S.J., Marshall, L.A., 1986. Thermal and mechanical constraints on mixing between mafic and silicic magmas. J. Volcanol. Geotherm. Res. 29, 99–124.
Stone, R., 2011. Vigil at North Korea's mount doom. Science 334, 584–588.
Sun, C.Q., Plunkett, G., Liu, J.Q., Zhao, H.L., Sigl, M., McConnell, J.R., Pilcher, J.R., Vinther, B., Steffensen, J.P., Hall, V., 2014a. Ash from Changbaishan Millennium eruption recorded in Greenland ice: implications for determining the eruption's timing and impact. Geophys. Res. Lett. 41, 694–701.
Sun, C.Q., You, H.T., Liu, J.Q., Li, X., Gao, J.N., Chen, S.S., 2014b. Distribution, geochemistry and age of the Millennium eruptives of Changbaishan volcano, Northeast China - a review. Front. Earth Sci. 8, 216–230.
Sun, C.Q., Liu, J.Q., You, H.T., Nemeth, K., 2017. Tephrostratigraphy of Changbaishan volcano, Northeast China, since the mid-Holocene. Quat. Sci. Rev. 177, 104–119.
Sun, C.Q., Wang, L., Plunkett, G., You, H.T., Zhu, Z.Y., Zhang, L., Zhang, B., Chu, G.Q., Liu, J.Q., 2018. Ash from the Changbaishan Qixiangzhan eruption: a new early Holocene marker horizon across East Asia. Geophys. Res.-Sol. Ea. 123, 6442–6450.
Townsend, M., Huber, C., 2020. A critical magma chamber size for volcanic eruptions. Geology 48, 431–435.
Wang, W., Chen, Q.F., 2017. The crust S-wave velocity structure under the Changbaishan volcano area in Northeast China inferred from ambient noise tomography. Chin. J. Geophys. 60, 3080–3095 (in Chinese with English abstract).
Wei, H.Q., Liu, G.M., Gill, J., 2013. Review of eruptive activity at Tianchi volcano, Changbaishan, Northeast China: implications for possible future eruptions. Bull. Volcanol. 75, 1–14.
Wotzlaw, J.F., Bindeman, I.N., Watts, K.E., Schmitt, A.K., Caricchi, L., Schaltegger, U., 2014. Linking rapid magma reservoir assembly and eruption trigger mechanisms at evolved Yellowstone-type supervolcanoes. Geology 42, 807–810.
Wu, J.P., Ming, Y.H., Zhang, H.R., Liu, G.M., Fang, L.H., Su, W., Wang, W.L., 2007. Earthquake swarm activity in Changbaishan Tianchi volcano. Chin. J. Geophys. 50, 1089–1096 (in Chinese with English abstract).
Xu, J.D., Liu, G.M., Wu, J.P., Ming, Y.H., Wang, Q.L., Cui, D.X., Shangguan, Z.G., Pan, B., Lin, X.D., Liu, J.Q., 2012. Recent unrest of Changbaishan volcano, Northeast China: a precursor of a future eruption? Geophys. Res. Lett. 39, L16305.
Xu, J.D., Pan, B., Liu, T.Z., Hajdas, I., Zhao, B., Yu, H.M., Liu, R.X., Zhao, P., 2013. Climatic impact of the Millennium eruption of Changbaishan volcano in China: new insights from high-precision radiocarbon wiggle-match dating. Geophys. Res. Lett. 40, 54–59.
Yang, L.K., Wang, F., Feng, H.L., Wu, L., Shi, W.B., 2014. $^{40}Ar/^{39}Ar$ geochronology of Holocene volcanic activity at Changbaishan Tianchi volcano, Northeast China. Quat. Geochronol. 21, 106–114.
Yi, J., Wang, P.J., Shan, X.L., Wang, H.F., Sun, S., Chen, H.C., 2019. Lahar deposits generated after the Millennium eruption of the Changbaishan Tianchi volcano in the Erdaobaihe River system, China. J. Volcanol. Geoth. Res. 380, 1–18.
Yin, J.H., Jull, A.J.T., Burr, G.S., Zheng, Y.G., 2012. A wiggle-match age for the Millennium eruption of Tianchi Volcano at Changbaishan, Northeastern China. Quat. Sci. Rev. 47, 150–159.
Yin, J.H., Zheng, Y.G., Liu, Y.X., 2005. The radiocarbon age of carbonized wood in Tianchi volcano, Changbaishang mountain and its implication. Seismology and Geology 27, 83–88 (in Chinese with English abstract).
Zhang, M.L., Guo, Z.F., Cheng, Z.H., Zhang, L.H., Liu, J.Q., 2015. Late Cenozoic intraplate volcanism in Changbai volcanic field, on the border of China and North Korea: insights into deep subduction of the Pacific slab and intraplate volcanism. J. Geol. Soc. 172, 648–663.
Zhang, M.L., Guo, Z.F., Liu, J.Q., Liu, G.M., Zhang, L.H., Ming, L., Zhao, W.B., Ma, L., Sepe, V., Ventura, G., 2018. The intraplate Changbaishan volcanic field (China/North Korea): a review on eruptive history, magma genesis, geodynamic significance, recent dynamics and potential hazards. Earth-Sci. Rev. 187, 19–52.
Zhao, D.P., Liu, L., 2010. Deep structure and origin of active volcanoes in China. Geosci. Front. 1, 31–44.
Zheng, X.S., Xu, X.X., Xu, D.M., 1998. Geology and genetic significance of the Laohudong stage activity of Tianchi volcano, Changbaishan area. China. Sci. Geol. Sin. 33, 426–434 (in Chinese with English abstract).
Zhu, H.X., Tian, Y., Zhao, D.P., Li, H.H., Liu, C., 2019. Seismic structure of the Changbai intraplate volcano in NE China from joint inversion of ambient noise and receiver functions. J. Geophys. Res.-Sol. Ea. 124, 4984–5002.
Zou, H.B., Fan, Q.C., Zhang, H.F., 2010. Rapid development of the great Millennium eruption of Changbaishan (Tianchi) Volcano, China/North Korea: evidence from U–Th zircon dating. Lithos 119, 289–296.
Zou, H.B., Fan, Q.C., Zhang, H.F., Schmitt, A.K., 2014. U-series zircon age constraints on the plumbing system and magma residence times of the Changbai volcano, China/North Korea border. Lithos 200-201, 169–180.